Submitted to:	U.S. Department of Energy
Report:	Research Performance Progress Report (RPPR)
Award #:	DE-EE0008204
Award Type:	DOE SSL
Prime Recipient:	University of California Santa Barbara Materials Department Santa Barbara, CA 93106-5050
Prime Recipient Type:	Public University
Project Title:	High Performance Green LEDs for Solid State Lighting
Primary Investigator(s):	James S. Speck and Shuji Nakamura
Prime Recipient DUNS #:	

Summary

The development of white LEDs for solid state lighting (SSL) has been driven in recent years by phosphor converted LEDs (pc-LEDs). However, losses (known as Stokes' losses) between the blue pump LED and phosphor impose a fundamental efficiency limit of ~300 lm/W on pc-LEDs. White light can also be generated from color mixed LEDs (cm-LEDs), which employ red, green, blue, and amber LEDs and have a fundamental efficiency limit of ~400 lm/W. Efficient group III-nitride materials are used for the blue LED, while efficient group III-phosphide materials are used for the red LED component. Currently, the poor efficiency of green and amber LEDs (i.e. the "green gap") is the primary limitation for cm-LEDs.

Relative to nitride-based blue LEDs, green and amber nitride LEDs suffer from lower radiative recombination rates and higher nonradiative recombination rates, which ultimately lead to reduced internal quantum efficiency (IQE). The IQE represents the portion of all electron-hole recombination events that result in a photon. In addition, long-wavelength LEDs have lower electrical efficiency (EE) compared to their blue counterparts. Addressing the green gap, would ultimately enable cm-LEDs that rival or exceed the performance of pc-LEDs.

Our project focused on III-nitride materials growth and characterization, device fabrication and testing, and semiconductor physics to understand efficiency limitations of green LEDs and develop solutions to these challenges. Insights gained during our research has led to novel long-wavelength LED designs which will enable efficient solid-state lighting.

Accomplishments

During this project, we made significant progress in identifying and addressing the sources of reduced efficiency in nitride c-plane green LEDs. Using a combination of experimental and simulation-based methods, we demonstrated that the quantum wells (QWs) of green LEDs are the primary internal barrier to carrier transport. We also investigated the transport differences between green and blue LEDs. From our findings, we pursued several LED designs to engineer around the difficulties associated with growing efficient green LEDs.

In one of our early experiments targeted at understanding the poor electrical efficiency of green LEDs, we examined the role of QW number. Experimentally, we grew an LED series by MOCVD with the number of QWs varying from 1 to 7. We observed a systematic increase in voltage, and thus decrease in EE, with the addition of each QW. Trends in LED electrical properties obtained from 3D simulations, which account for alloy disorder, are in agreement with experimental data. Importantly, this agreement was achieved without adjusting polarization parameters from their known values, which is a common practice. From these experimental and simulation results, we proposed that polarization induced barriers at the GaN/InGaN (lower barrier/QW) interfaces and sequential filling of QWs both contribute significantly to the excess applied voltage in multiple QW green LEDs.

To further investigate the role of polarization barriers and sequential filling, we performed a simulation study to elucidate the impact of QW number in blue versus green LEDs with either one or five QWs. For green LEDs, increasing the QW number from one to five resulted in an increase in applied diode bias of 1.9 V at 20 A cm^{-2}. However, for the blue LED, increasing the QW number led to a smaller difference of only 0.45 V. By artificially turning off the polarization fields in the simulation, we discovered that sequential band filling of the QWs due to large band

offsets also contributes to the large excess voltage simulated for the five QW green LED. Approximately half of the 1.9 V penalty can be attributed to polarization barriers while the other half can be attributed to sequential filling. In contrast, when the polarization is turned off for the blue LED case, the voltage penalty of going from one to five QWs is only ~0.05 V. These results shed light on a previously unidentified mechanism that can explain the reduced electrical efficiency of green LEDs relative to blue.

To address the large polarization barriers present in multiple QW green LEDs, we explored advanced designs such as the use of InGaN quantum barriers and polarization screening. However, we identified V-defect engineering as a particularly promising approach to achieve efficient long wavelength nitride LEDs. A first indication of the efficacy of V-defect engineering came from an experimental study in which we increased the superlattice period and observed a decrease in forward voltage and an increase in power. We now attribute the device improvement to the nucleation of V-defects in the superlattice which then propagate up through the active region. V-defects can improve LED efficiency by enhancing hole injection. This is possible due to the lower polarization charge densities at the InGaN/GaN and AlGaN/GaN interfaces on the semipolar $\{10\bar{1}1\}$ sidewalls relative to the planar region. By utilizing a high period superlattice and increasing the V-defect density, we demonstrated improvement in forward voltage of green LEDs. Additionally, we used advanced characterization methods—including transmission electron microscopy, energy dispersive X-ray spectroscopy, atom probe tomography, and scanning near-field optical microscopy—to study the structure of V-defects and their impact on LED optical and electrical properties. Our initial efforts on V-defect engineering during this project have paved the way for UCSB to demonstrate high WPE long-wavelength LEDs.

Project Activity

In this section, we summarize the project activities for the entire period of funding. For each of the five tasks associated with this project, we include information such as the original hypotheses, approaches used, and findings. Where applicable, we refer to published journal articles which contain the relevant scientific and technical information.

Task 1. Engineering against SRH

TMI:TEG flow ratio

We performed InGaN QW optimization by varying the indium precursor (TMI) to gallium precursor (TEG) flow ratio. Our hypothesis was that a higher TMI:TEG ratio would allow for higher QW growth temperature. The methods used include MOCVD growth of samples interrupted at the active region surface, AFM, and photoluminescence (PL) measurements. Our reference InGaN QW growth conditions were 70 sccm TMI and 27 sccm TEG and the growth temperature was 800 °C. For a given TEG flow, we investigated higher TMI flows and observed a degradation in the morphology of the active region, as measured by atomic force microscopy (AFM). However, this was accompanied by an increase in the peak PL wavelength. At the same growth temperature of 800 °C, when the TMI:TEG ratio was increased from 70:27 (low In/Ga) to 120:10 (high In/Ga), there was a red shift in the PL wavelength from ~540 nm to ~590 nm. When the high In/Ga ratio QW conditions were used in conjunction with a higher growth temperature, the wavelength blue shifted. Our findings indicate that by increasing the TMI to TEG ratio, the QW growth temperature can be increased by ~10 °C to achieve the same peak wavelength while maintaining smooth morphology (Figure 1).

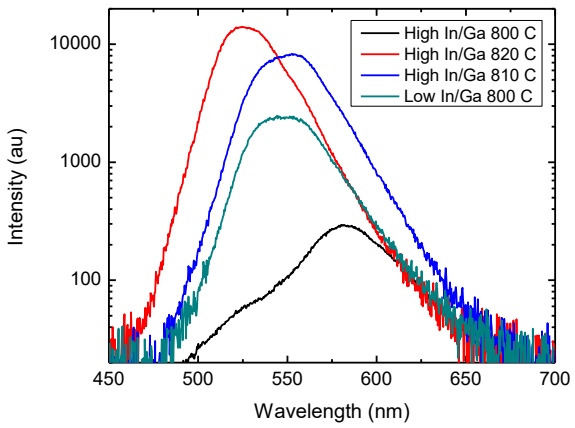

Figure 1. Normalized photoluminescence spectra for full LED samples with a TMI/TEG ratio of 70/27 at 800 ºC and a TMI/TEG ratio of 120/10 at temperatures of 800 ºC, 810 ºC, and 820 ºC.

Role of Superlattice

To reduce SRH nonradiative recombination, we also explored the role of the pre-active region InGaN/GaN superlattice (SL). Our hypothesis was that increasing the period of the superlattice would result in higher power LEDs with no change in voltage. Our approach involved MOCVD growth of LEDs with varying SL period, testing of processed LEDs, and electron emission spectroscopy (EES). When the SL period was increased from 0x to 30x, we observed an increase in power and a decrease in voltage (Figure 2). We now understand that the lower voltage with increasing period can be attributed to V-defects; we elaborate on this finding in **Task 4. Voltage Reduction**. From EES data, we identified a new high energy peak 2.3 eV about the Γ peak (Figure 3). The normalized integrated intensity of this peak was large for the 0x SL sample but decreased significantly for the 10x SL sample (Figure 4). There was then a smaller reduction in integrated intensity of the peak from the 10x to the 20x sample and the intensity of the peak was negligible for the 30x sample. We also observed a decrease in normalized integrated intensity of the newly discovered high energy with increasing temperature. This is similar to the trend seen for the L valley, indicating that the high energy peak possibly has an Auger-like origin. We propose that increasing the SL period results in a reduction of trap-assisted Auger recombination centers. Our group has described in more detail this mechanism in a recent publication [Myers 2020].

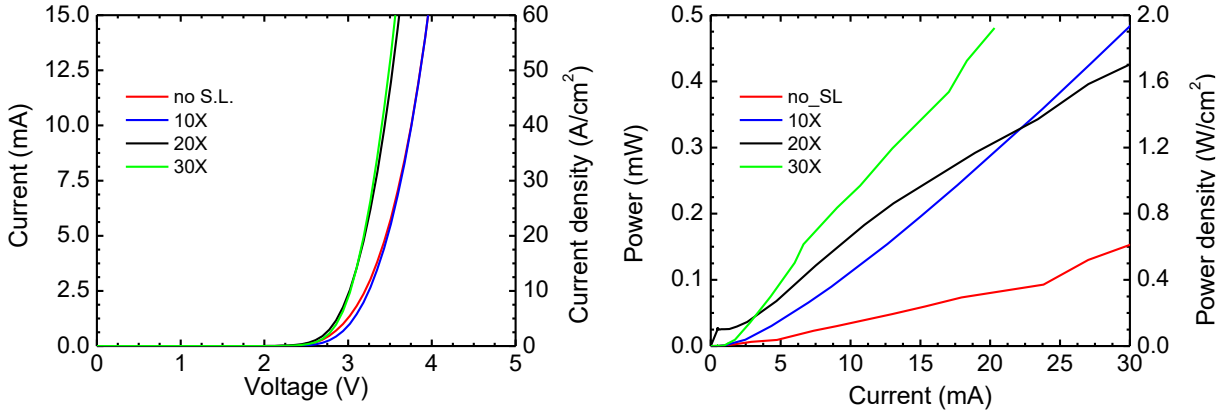

Figure 2. J-V curves (left) and L-J curves (right) for green LEDs with a 0x, 10x, 20x, or 30x period InGaN/GaN superlattice. Increasing the period of the superlattice resulted in in lower voltage and higher power LEDs . The samples were fabricated to LEDs with Pd/Au p-contacts and measurements were performed on-wafer, with power collected from the backside using a photodiode.

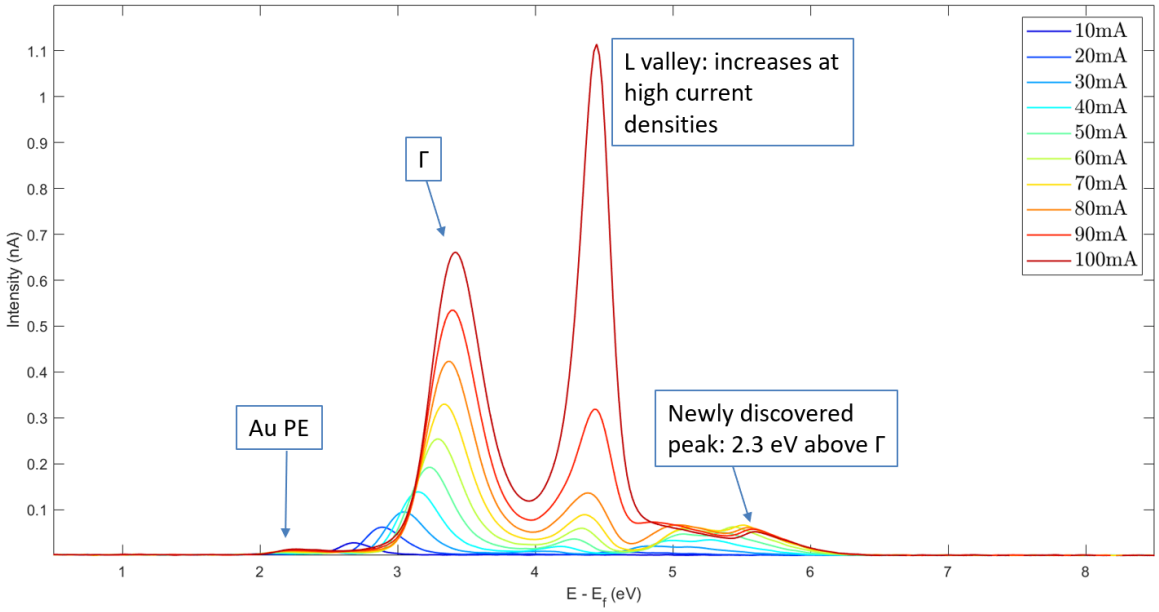

Figure 3. EES spectrum of 0x SL sample under 40% duty cycle from 10 mA to 100 mA. A new high energy peak 2.3 eV about Γ was discovered.

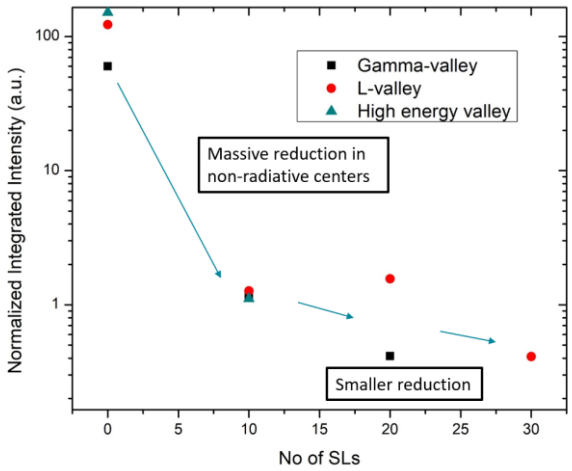

Figure 4. Normalized integrated intensity of the Γ, L, and high energy valleys for LEDs with varying SL period. From 0x to 10x, there is a very large reduction in peak intensity. A smaller reduction is seen when increasing the SL period to 20x and 30x.

Task 2. Advanced Design

The research for Task 2 utilized a novel device simulation tool based on landscape theory. Using this tool, we performed 3D simulations to explore LED device designs which reduce internal potential barriers to electron and hole transport and achieve balanced carrier injection.

Green vs. Blue LEDs: Role of QW Number

To understand the origin of excess voltage in green LEDs, we performed 1D and 3D simulations of green LEDs with varying number of QWs. We investigated the role of internal fields by artificially setting the polarization fields to 0%. These same simulations were repeated for blue LEDs to identify the role of indium content. Our findings have been accepted for publication in Journal of Applied Physics [Lheureux 2020].

InGaN Alloy Quantum Barriers

InGaN alloy quantum barriers (QBs) were examined using 1D and 3D simulations as a potential path to low voltage green LEDs with decreased internal potential barriers. Our hypothesis was that InGaN barriers would lead to lower voltage. We simulated structures with varying indium content in the quantum barriers and the J-V curves showed that increasing indium led to lower voltage (Figure 5). To understand the J-V trends, we calculated the electron-hole spatial overlap (EHSO) and found that the bias at which a given EHSO is reached, decreases with increasing QB In composition (Figure 6). This trend is attributed to a decrease in the electric field in the QW due to the reduced polarization discontinuity at the QW/QB interface when using InGaN barriers relative to GaN barriers. With a reduced electric field, the spatial overlap of electrons and holes is increased. We also found that the percolation path of carriers through the barriers is an important 3D behavior that cannot be accounted for in usual 1D simulations. Figure 7 shows the electrons current map in the XZ plane at y = 15 nm for single QW structures with either GaN barriers or InGaN barriers with 7% In. In the case of GaN barriers, the electron injection through the barriers

below the QW is relatively uniform while clear percolative paths are visible in the structure with InGaN barriers. The hypothesis that these percolative paths also help in reducing the turn on voltage. This is a phenomenon that we are currently investigating further and plan to publish a comprehensive study comparing InGaN and GaN QBs.

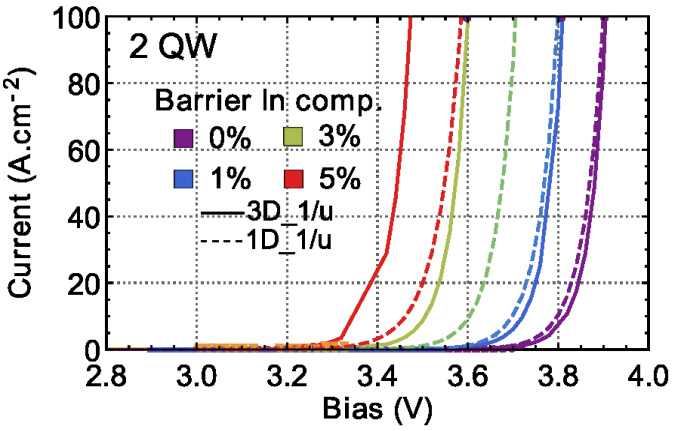

Figure 5. Comparison of J-V curves from 1D and 3D simulations of green LEDs with $In_xGa_{1-x}N$ QBs of varying In composition and 2 QWs.

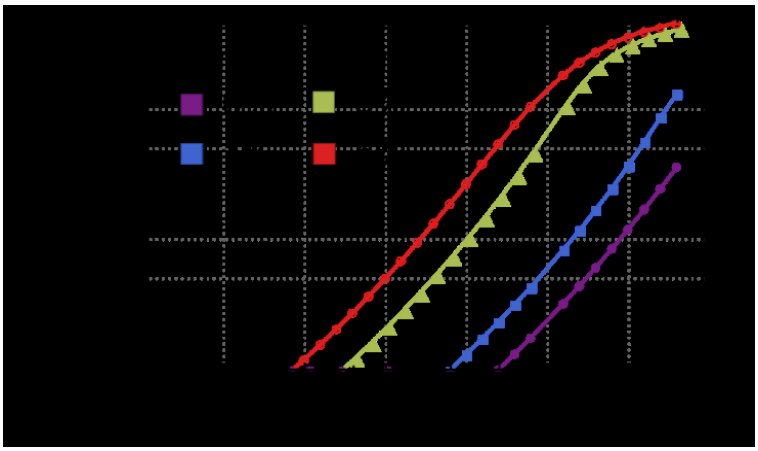

Figure 6. Electron and hole spatial overlap as a function of bias for 1 QW LEDs with different InGaN barrier compositions.

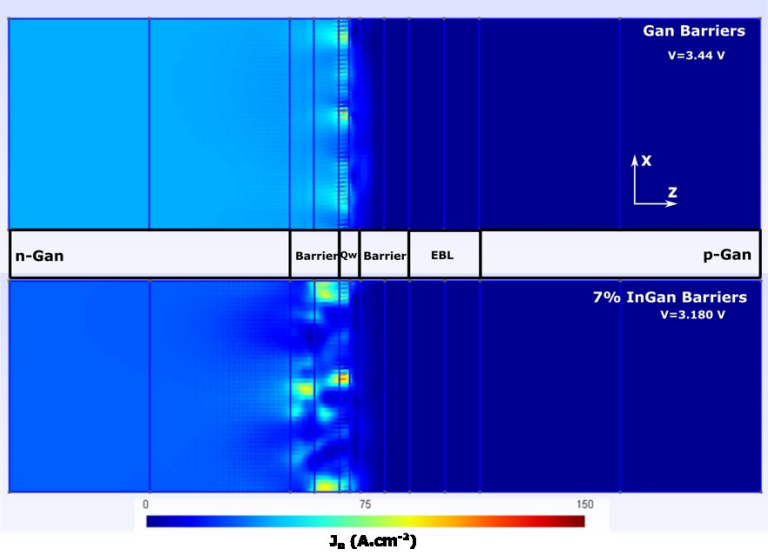

Figure 7. 2D electron current maps of a 0% and 7% indium InGaN barrier taken in the middle of the structure (y = 15 nm) at J = 1 A cm^{-2}.

Polarization Field Screening

Using advanced design, we explored LED structures with different doping profiles in proximity to the active region. We first examined a single QW structure with an n-type doped layer on the n-side of the QW and a p-doped layer on the p-side of the QW. A schematic of the structure is shown in Figure 8. The doping in these layers was varied equally and concurrently from $1x10^{19}$ cm^{-3} to $1x10^{20}$ cm^{-3}. From the simulated J-V curves in Figure 8, we observe a decrease in voltage as the doping is increased; however, beyond $7x10^{19}$ cm^{-3}, there is no additional improvement in forward voltage. As the doping of the layers is increased, we hypothesize that the electric field in the QW becomes progressively screened and full screening is achieved at $7x10^{19}$ cm^{-3}. When the quantum barriers are undoped, large energy barriers due to polarization charges are present and prevent carrier flow into the active region. This is due in particular to large polarization-induced electric fields present in strained c-plane InGaN/GaN quantum wells. This electric field is well known to diminish the electron-hole wavefunction overlap through the quantum confined Stark effect. In our case, this field is also responsible for these energy barriers. When the doping concentration is increased, the energy barrier is decreased and allows carriers to more easily reach the active region where they can recombine, resulting in a lower V_F.

We also found that this "polarization field screening" approach can help to balance carrier injection. In Figure 9, we plot the carrier density of electrons and holes in the QW as a function of bias for single QW structures with no doping, $1x10^{19}$, $3x10^{19}$, or $8x10^{19}$ cm^{-3}. We observe that for all cases except the $8x10^{19}$ cm^{-3} doped structure, the electron density is higher than the hole density. Once the doping becomes large enough to screen the polarization field, the hole carrier density exceeds the electron density. This demonstrates how polarization field screening should be explored for achieving balanced carrier injection into the QWs of green LEDs. It is possible that symmetric doping is not ideal and a different n- and p-doping level in the barrier will produce better results.

In addition to the single QW structure, we performed 3D simulations on a 5 QW green LED structure where the first bottom barrier is highly n-doped and the last top barrier is highly p-

doped. Again, we symmetrically doped the structure and varied the doping levels concurrently. A schematic of the structure is shown in Figure 10. Similar to the single QW case, increasing the doping of these layers leads to a reduction in the forward voltage which can be seen in the simulated J-V curves in Figure 10. For the multiple QW LED, there is an improvement in voltage up to $5x10^{19}$ cm^{-3}. We do not expect that doping in this case allows for complete screening but that it still helps to reduce the polarization induced barriers for carrier injection into the QWs.

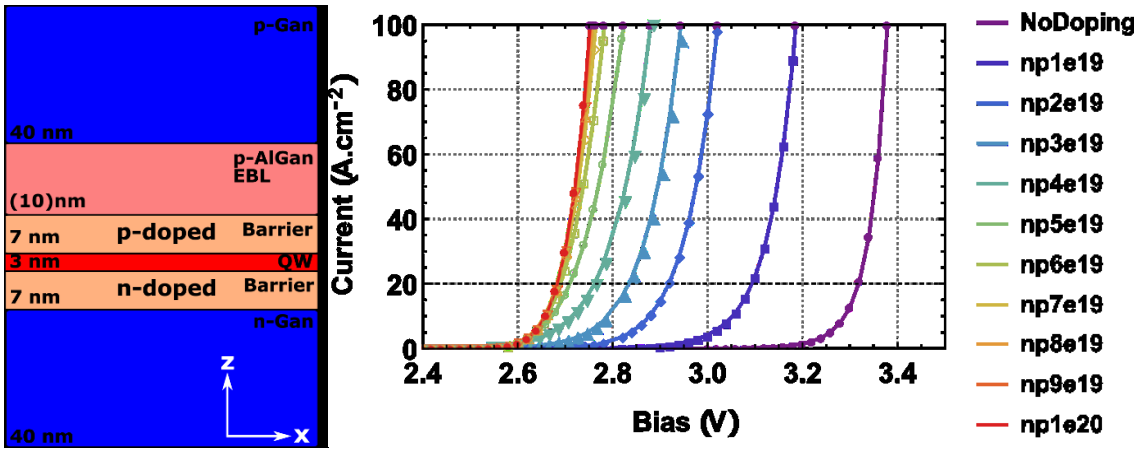

Figure 8. Single QW LED structure used in the 3D simulations. The first (last) QW barrier is n (p) doped. The simulated J-V curves for different doping densities are plotted and a decrease in V_F is observed with increasing doping.

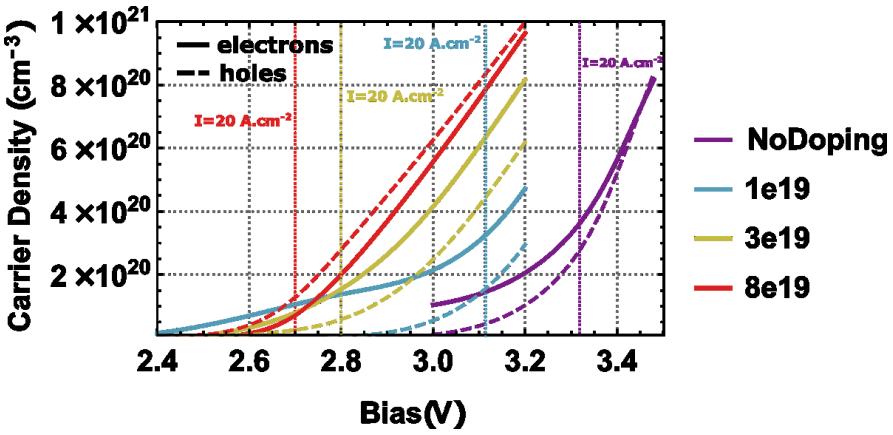

Figure 9. Carrier density of electrons (solid) and holes (dashed) as a function of bias for single QW LED structures with varied barrier doping levels.

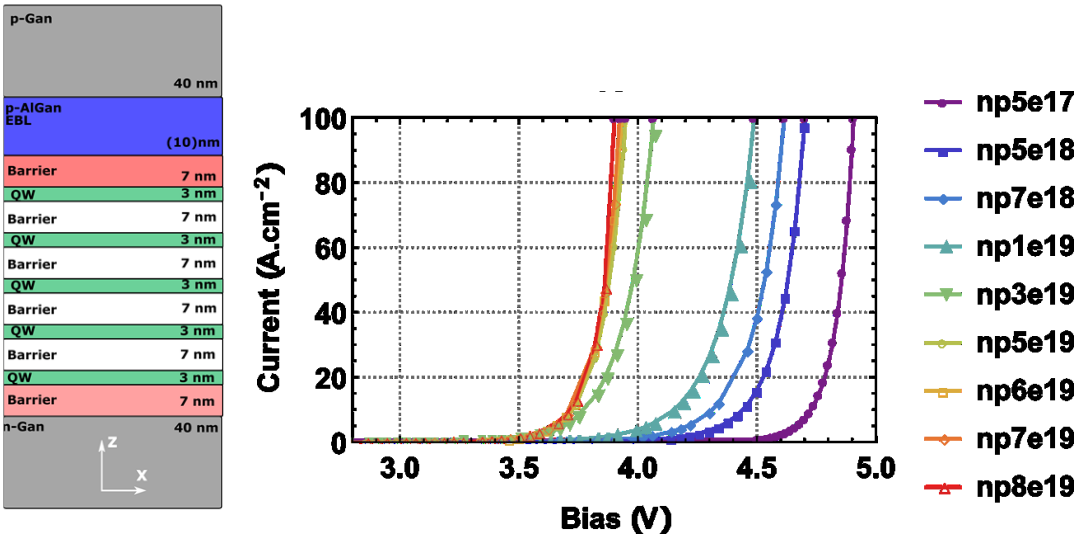

Figure 10. 5 QW LED structure used in the 3D simulations. The first (last) QW barrier is n (p) doped. The simulated J-V curves for different doping densities are plotted and a decrease in V_F is observed with increasing doping.

Task 3. Polarization Engineering

InGaN Alloy Quantum Barriers

The approach proposed here is to improve carrier transport in the active region by using InGaN, rather than GaN, quantum barriers. Incorporating alloy quantum barriers may present an opportunity to improve vertical transport in green LEDs and lead to lower voltage, as demonstrated by our 3D simulation results described in **Task 2. Advanced Design**. Optimization of the barrier thickness and indium fraction, while maintaining abrupt interfaces to avoid loss of confinement in the QWs is required. Additional advantages of using InGaN barriers include lower barrier height due to smaller band gap, reduced polarization discontinuity between quantum wells and barriers, and the surfactant effect associated with flowing In during MOCVD GaN growth.

Preliminary experiments were carried out for 1, 3, and 5 QW LEDs. Lower V_F values were measured when using quantum barriers consisting of 2 nm $Al_{0.05}Ga_{0.95}N$ and 6 nm $In_{0.04}Ga_{0.96}N$ compared to 2 nm $Al_{0.05}Ga_{0.95}N$ and 6 nm GaN (Figure 11). Relative to their counterparts with GaN barriers, a blue shift in emission wavelength was observed for LEDs with InGaN barriers. The trend for LEDs with GaN barriers was an increase in wavelength with QW number; however, the wavelength was relatively independent of QW number for InGaN barrier samples. If InGaN QBs are to be incorporated into green LEDs, the indium composition in the quantum wells will need to be increased to achieve 525 nm emission. These LEDs were also characterized using APT; these data are presented in **Task 5. Advanced Characterization**.

In addition to studying the role of InGaN quantum barriers experimentally in LEDs, we grew structures to characterize transport between QWs when different types of QBs were used. Specifically, we examined vertical transport of holes to deeper QWs for the case of InGaN barriers of different indium composition, GaN barriers, and AlGaN barriers. These results were published in Applied Physics Express [Yapparov 2020a].

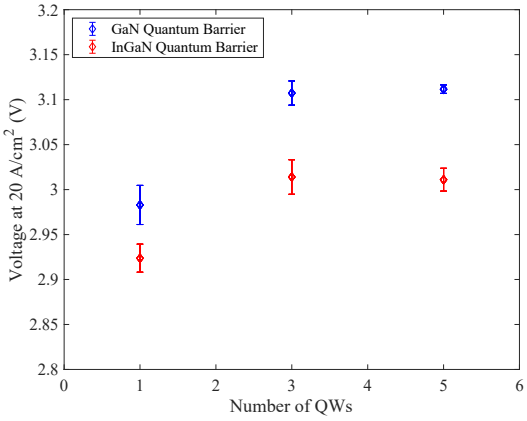

Figure 11. Experimental V_F measured at 20 A cm^{-2} for LEDs with 1, 3, or 5 QWs and either GaN or InGaN quantum barriers. APT measurements of a 3/5 QW LED with InGaN QBs (b) 3D reconstruction of the active region and (c) 1D concentration profile of In and Al measured along the [0001] direction.

Polarization Field Screening: Blue LEDs

We experimentally investigated polarization field screening for single QW LEDs. As a first step, we explored screening in blue LEDs which are easier to grow thick InGaN QWs and have a smaller polarization field to screen. Our optimization efforts on blue LEDs will be relevant for our continued work on screening in green LEDs. Our hypothesis was that a thick polarization field screened blue LED would have lower droop, and thus a higher EQE at high current density, compared to a thin unscreened blue LED.

Our first finding was that the doping levels of the screening layers should be as low as possible to avoid morphological degradation and high SRH recombination but high enough to screen the polarization field to ensure large wavefunction overlap, especially for thick SQW LEDs. The final optimized doping level of the screening layers for a 9-nm thick SQW LED was approximately 4.5x10^{19} cm^{-3} and 1.5x10^{19} cm^{-3} for the p- and n-sides, respectively.

To demonstrate the effect of the screening layers on LEDs with different QW thickness, a series of LEDs were grown. The epitaxial structures of the active region of four blue LEDs are shown in Figure 12. The LEDs either have 3 nm or 9 nm SQW. Two LEDs have the heavily doped screening layers on both sides of the SQW while another two LEDs do not.

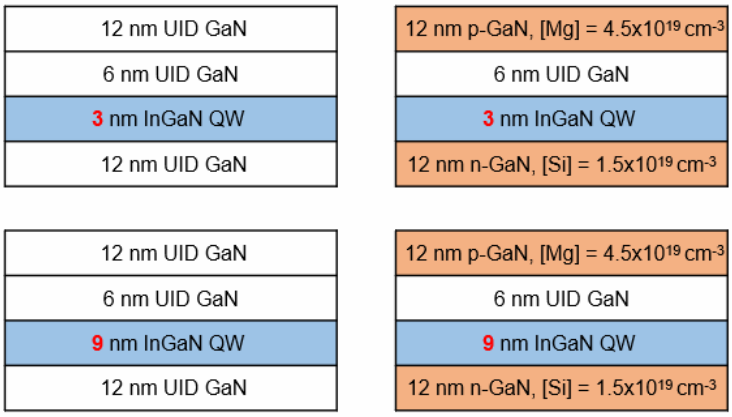

Figure 12. Schematic of the active region structure for the four blue SQW LEDs grown in the polarization field screening series.

The relative EQE of the LEDs are shown in Figure 13. The unscreened LED with a 3 nm SQW has the highest peak EQE. However, for the unscreened LEDs, as the QW thickness increases from 3 nm to 9 nm, the efficiency of the LED decreases significantly. This is not a surprising result. The unscreened LED with a thick LED has a very small (<1%) wavefunction overlap due to the large spatial separation of the electron and hole wavefunctions in the thick QW. Therefore, it should greatly lower the recombination rates and efficiency.

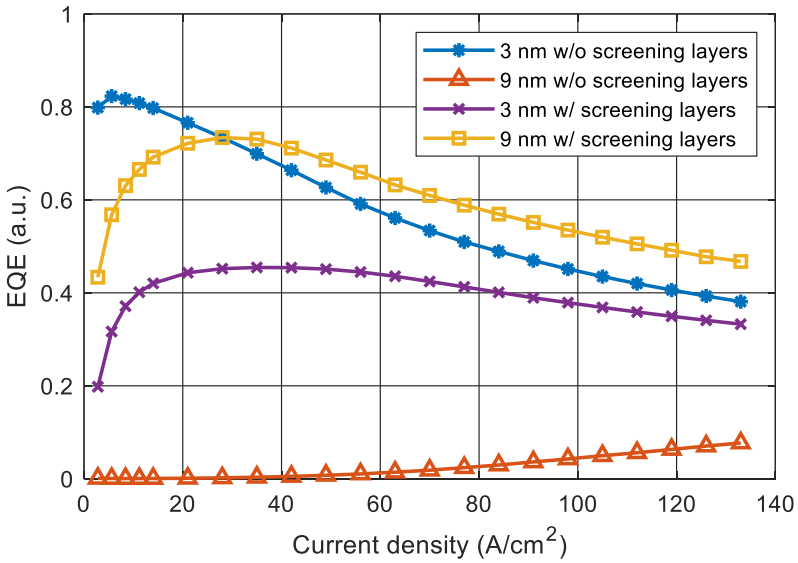

Figure 13. Quick test relative EQE versus current density for 3 nm and 9 nm SQW blue LEDs with and without screening layers in the active region.

However, the inclusion of the screening layers into the 9 nm SQW LED improves the efficiency significantly. The heavily doped screening layers seem to screen the polarization field and recover the wavefunction overlap. Although its peak EQE is lower than that of the unscreened 3 nm SQW LED, the peak happens at higher current density. Additionally, at high current density,

the screened 9 nm SQW LED outperforms the unscreened 3 nm SQW LED. This is expected for a thick SQW LED. Due to the larger volume of the active region (thicker InGaN QW), the carrier concentration in the QW at the same current density should be lower than that of its thin QW counterpart. This should delay the efficiency droop onset and improve the efficiency at high current density.

Lastly, for completion, the EQE of a screened 3 nm SQW LED is also shown in the same figure. The inclusion of the screening layers into the 3 nm SQW LED seems to deleteriously impact the performance of the LED. A 3 nm SQW LED is unlikely to benefit from the field screening brought forth by the screening layers. The thin SQW LED should have reasonable wavefunction overlap due to the spatial confinement of the narrow well. In fact, the proximity of those heavily doped layers to the QW might introduces more non-radiative recombination centers (NRC) into the QW which negatively impacts the LED's performance.

Our findings indicate that heavily doped screening layers are essential to thick SQW blue LEDs but negatively impact the performance of thin SQW LEDs. However, the situation might not be the same for long wavelength LEDs (e.g. green and yellow LEDs). Due to the high indium content in the QW, the larger strain induces even larger polarization field in the QW. Partial screening or full screening of the polarization field in those devices might be important in improving their quantum efficiency.

Lastly, we grew blue LEDs for full processing and packaging to measure the absolute EQE. An optimized screened 10 nm thick SQW LED and an unscreened (reference) 3 nm thick SQW LED were grown. For the screened (unscreened) LED, the 10 nm (3 nm) thick SQW and the 6 nm UID GaN cap were sandwiched between a 13 nm thick n-GaN screening layer (UID GaN) and a 10 nm thick p-GaN screening layer (UID GaN).

The two samples were then processed into LEDs using standard contact lithography. The LEDs were singulated into a 1×1.3 mm^2 dice by dicing. After singulation, they were mounted onto silver headers, wire bonded with Au wires, and encapsulated in silicon. The LEDs were then tested under continuous-wave conditions in a calibrated integrating sphere with a MAS 40 spectroradiometer. The measured EQE and the EL peak wavelength of the devices are shown in Figure 14. The EQE of the unscreened 3 nm LED peaks around 10 A/cm^2 while the EQE of the screened 10 nm LED are consistent between 20-80 A/cm^2. Although the 3 nm LED has a higher peak EQE, at high current density (>50 A/cm^2), the screened 10 nm LED is more efficient because it has a much smaller efficiency droop due to a thicker quantum well (larger active volume). The EL peak wavelength of the unscreened 3 nm LED blue-shifts considerably while the EL peak wavelength of screened 10 nm LED is almost unchanged across the entire measured range. However, the EL wavelength of the screened device is shorter due to a reduced internal electric field in the QW.

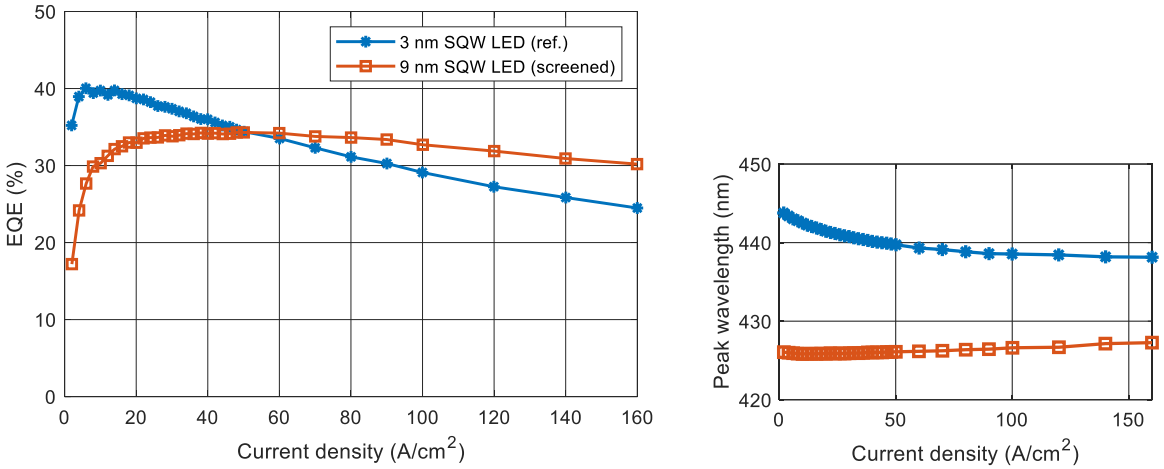

Figure 14. Left: EQE versus current density for unscreened 3 nm and screened 10 nm SQW blue LEDs. LEDs were packaged and measured in an integrating sphere. Right: EL peak wavelength versus current density for unscreened 3 nm (blue curve) and screened 10 nm (orange curve) SQW blue LEDs. At all current densities, the peak wavelength of the screened LED was blue shifted relative to the unscreened LED.

Polarization Field Screening: Green LEDs

Our work on polarization field screening in green LEDs closely followed the approach we took for blue LEDs. Similar to blue, we began by establishing a baseline MQW structure and then transitioning to a SQW structure. For the first samples studied, we grew a SQW green LED with 12 nm UID GaN interlayers and 12 nm UID GaN barrier layers (Figure 15(a)). We then introduced Mg and Si dopants into the 12 nm barrier layers while keeping 12 nm thick interlayers (Figure 15(b)). Finally, we moved the Si-doped barrier directly below the QW and reduced the p-side GaN interlayer thickness from 12 nm to 6 nm (Figure 15(c)).

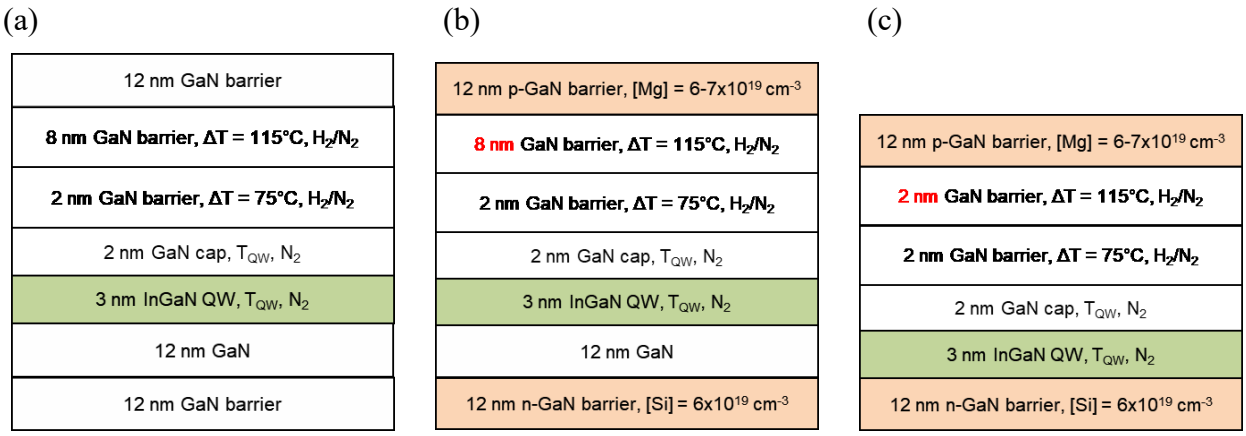

Figure 15. Schematic of SQW green LED active region for samples with (a) no Si- or Mg-doped barrier layers, (b) doped barrier layers and 12 nm thick UID GaN interlayers on either side of the QW, and (c) doped barrier layers with no n-side GaN interlayer and a 6 nm p-side GaN interlayer.

The next growth studies that were carried out for field screening in green LEDs was varying the doping level in the Mg- and Si-doped barriers. We again grew a reference sample without

doped barriers. For the three structures with doped barriers, the Si-doped barrier was directly below the QW and the Mg-doped barrier was 6 nm from the QW. The Cp_2Mg and Si_2H_6 flows were then varied in the barriers to achieve different doping concentrations. Sample SQW D had flows of 0 sccm of Cp_2Mg and Si_2H_6, Sample SQW E had flows of 15 sccm Cp_2Mg and 2 Si_2H_6, Sample SQW F had flows of 10 sccm Cp_2Mg and 2 Si_2H_6, Sample SQW G had flows of 10 sccm Cp_2Mg and 1 Si_2H_6. The active region structures are shown in Figure 16.

The quick test EQE data for these samples are shown in Figure 17. From the reference sample with no doped barrier layers (SQW D), we saw a reduction in peak EQE and droop with the introduction of doped barriers as well as a blueshift of the peak wavelength at 20 mA. When the Cp_2Mg flow was reduced from 15 sccm to 10 sccm, there was little change in performance and a small redshift in the wavelength. When the Si_2H_6 flow was reduced, we saw a large improvement in EQE but greater droop and a 10 nm redshift at 20 mA relative to SQW F. We also tested several of the LEDs to compare the peak wavelength at low current (20 mA) and high current (134 mA). Interestingly, from low to high current, we saw the largest blueshift of 12 nm for the undoped SQW D structure. For SQW F, which we expect to have a high degree of screening, we saw no change in wavelength. Finally, for SQW G, which we expect to have partial screening, we observed a small blueshift of 4 nm.

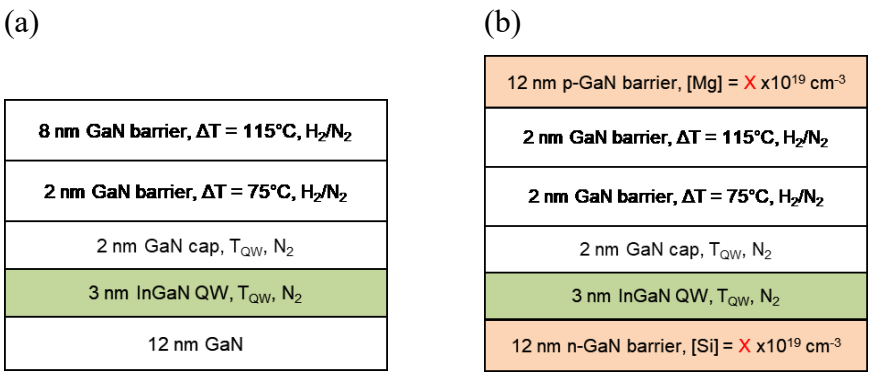

Figure 16. Schematic of SQW green LED active region for samples with (a) no Si- or Mg-doped barrier layers and (b) barrier layers doped at varying levels with no n-side GaN interlayer and a 6 nm p-side GaN interlayer.

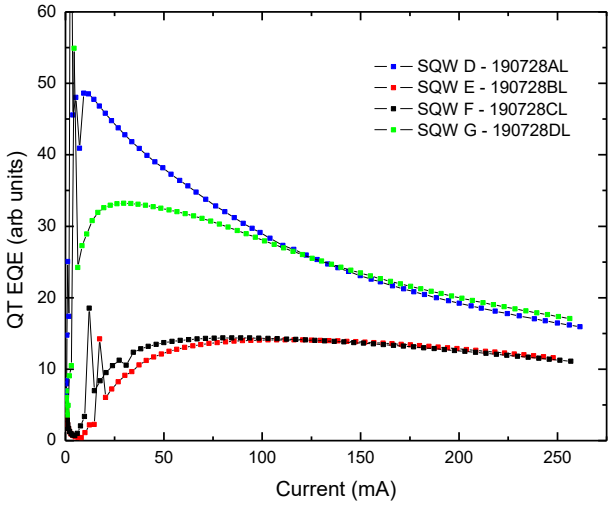

Sample	λ at 20 mA	λ at 134 mA
SQW D	512 nm	500 nm
SQW F	470 nm	470 nm
SQW G	480 nm	476 nm

Figure 17. Quick test EQE (in arbitrary units) versus current for SQW green LEDs with varying active region structures (top) and the wavelength of select samples at 20 mA and 134 mA (bottom).

Task 4. Voltage Reduction

Role of QW Number: Green LEDs

We demonstrated experimentally and through simulation that increased quantum well (QW) number in *c*-plane green LEDs contributes to excess driving voltage, and therefore reduced electrical efficiency. Experimentally, we grew an LED series with the number of QWs varying from 1 to 7 and observed a systematic increase in voltage with the addition of each QW. Trends in LED electrical properties obtained from 3D simulations, which account for the effects of random alloy fluctuations, agreed with experimental data. Agreement was achieved without the need for adjusting polarization parameters from their known values. From these results, we proposed that

the polarization induced barriers at the GaN/InGaN (lower barrier/QW) interfaces and the sequential filling of QWs both contribute significantly to the excess forward voltage in multiple QW *c*-plane green LEDs. These results were published in Physical Review Materials [Lynsky 2020].

V-defect Engineering

Nanchang University reported green and yellow LEDs with impressive wall-plug efficiency (WPE) [Jiang 2019]. The remarkable progress in the green, yellow and amber LEDs at Nanchang University can be attributed to progress in active region growth and circumventing the polarization-related barriers for hole injection into the QWs via the development of V-defects. LEDs with dominant wavelength ranging from 522 nm to 585 nm were reported. The WPE (at 20 A/cm^2) is 41.3% at 522 nm and gradually decreases to 11.6% at 585 nm. We have verified these results after receiving several packaged devices from Nanchang University.

One of the main factors that the group managed to achieve great WPE for their LEDs is the greatly reduced operating voltage, V_F. The reported forward voltage of the LEDs from Nanchang University decreases with increasing wavelength. At 20 A/cm^2, the voltage is 2.65 V at 522 nm and 2.30 V at 585 nm. Remarkably, the voltage is even lower than the average photon voltage V_{ph} at low current density (<2-3 A/cm^2).

The group attributes their low operating voltage to the V-defects (also referred to as V-pits) in their devices. V-defects usually form during low temperature *c*-plane GaN growth and nucleate on pre-existing threading dislocations. It consists of six $\{10\bar{1}1\}$ family planes which form an inverted hexagonal pyramid. The V-defects have been suggested to enhance the hole injection into the multi-quantum wells (MQWs) [Quan 2014, Wu 2014, Quan 2015]. The injection of carriers is easier through the sidewalls of V-defects than the planar region of the MQWs due to the thinner sidewalls and the semipolar facets, which reduce the polarization charge densities at the interfaces of the sidewall structure of V-pits. Additionally, it has also been suggested that threading dislocations can be self-screened by the formation of V-defects [Hangleiter 2005]. The thinner sidewalls of V-defects increase the potential barrier around each threading dislocation, preventing carriers from recombining non-radiatively at the defect.

The exciting results from Nanchang University show that LEDs with engineered V-defects have huge potential especially for LEDs with longer wavelength. This allows novel approaches for solving efficiency droop and achieving higher efficiency.

These findings on the beneficial role of V-defects are consistent with our previous results indicating that polarization barriers in green LEDs significantly contribute to a large ΔV_F [Lynsky 2020, Lheureux 2020]. The semipolar sidewalls of V-defects may then provide a lower polarization barrier for carrier injection into QWs relative to planar injection. A significant portion of the experimental research published on V-defects for voltage reduction is for GaN growth on silicon substrates, where TD densities are on the order of 10^9 cm^{-2}. These high TD densities in turn make it possible to realize LEDs with V-defect densities on the order of 10^9 cm^{-2}. For conventional GaN growth on sapphire substrates, TD densities are on the order of low 10^8 cm^{-2}, leading to lower V-defect densities.

In this work we systematically *increased* the TD density, and thus the V-defect density, in InGaN-based green LEDs grown on sapphire substrates by MOCVD. By increasing the V/III ratio

during high temperature UID GaN growth, higher densities of TDs and V-defects were achieved. From XRD rocking curve measurements, $\Delta\omega_{0002}$ remained constant while $\Delta\omega_{20\bar{2}1}$ increased significantly with NH_3 flow, indicating a negligible change in screw-component dislocations but a large increase in edge dislocations (Figure 18). By comparing the V-defect density at the top of the active region from SEM to the TD density from CL (Figure 19), it was observed that not all TDs opened into large V-defects (greater than ~150 nm across). After superlattice and active region growth, a significant population of TDs without V-defects, or with only small V-defects (less than ~150 nm across), still exist. A decrease in V_F from 3.07 V to 2.94 V with increasing V-defect density from 2.0×10^8 to 5.0×10^8 cm^{-2} was measured in fabricated LEDs (Figure 20). These findings agree with previous simulations and experiments which indicate that the semipolar sidewall QWs in V-defects provide a lower energy barrier for hole injection into deeper QWs due to the lower polarization charge densities at the InGaN/GaN and AlGaN/GaN interfaces. The opening of all TDs into large V-defects with well-defined sidewall structure is predicted to lead to further reduction in V_F as well as reduction in nonradiative recombination at TDs. The results presented here highlight the promise of V-defect engineering for voltage reduction in long wavelength III-nitride LEDs grown on sapphire substrates.

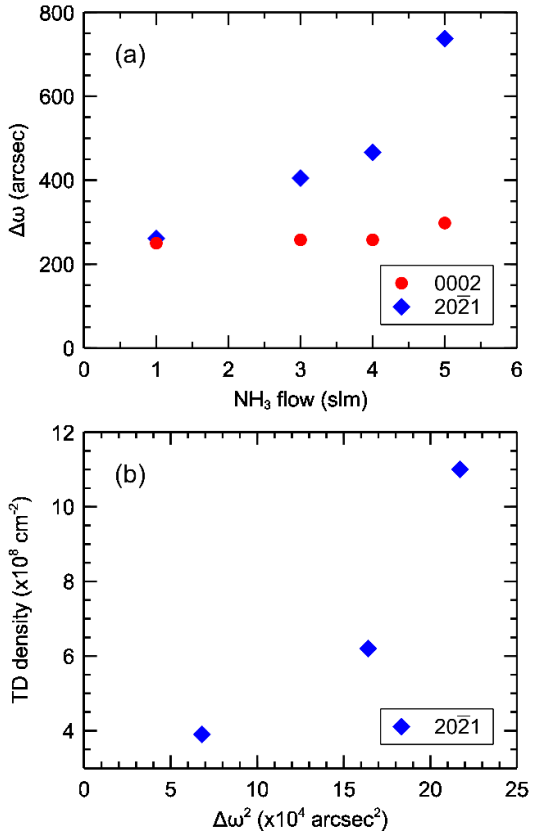

Figure 18. (a) Δω values from XRD ω-rocking curve scans of the 0002- and 20$\bar{2}$1-reflections. Measurements were taken on template samples grown with 1, 3, 4, or 5 slm NH_3 (samples GaN-1, GaN-3, GaN-4, and GaN-5, respectively).. (b) Dependence of TD density (as measured by CL) on $\Delta\omega^2_{20\bar{2}1}$ from XRD measurements of the GaN-3, GaN-4, and GaN-5 samples.

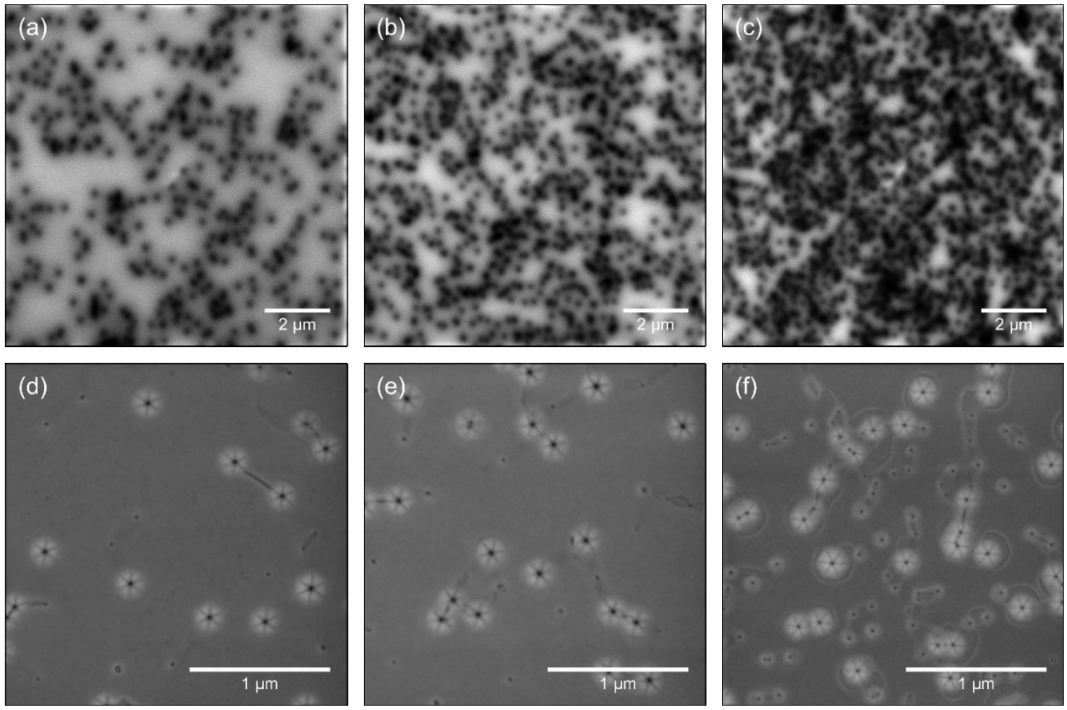

Figure 19. Panchromatic CL images (5 kV, 1.6 nA) of GaN template samples using (a) 3 slm (GaN-3), (b) 4 slm (GaN-4), and (c) 5 slm (GaN-5) NH_3. Secondary electron SEM images (2 kV) at the top surface of the active region for interrupted growth samples with (d) 3 slm (IG-3), (e) 4 slm (IG-4), and (f) 5 slm (IG-5) NH_3 flow.

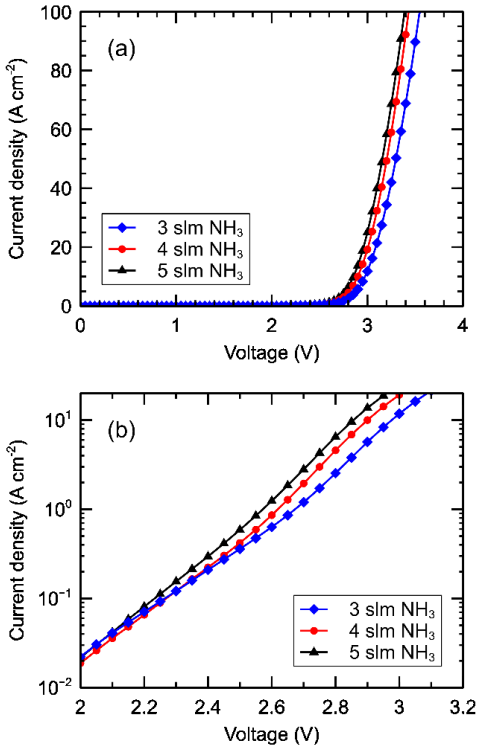

Figure 20. (a) J-V curves for LED samples with varying template NH_3 flow and thus threading dislocation and V-defect densities. (b) Reduced view of semi-log J-V curves to emphasize the trend in V_F at low J, where the series resistance contribution is minimal.

Task 5. Advanced Characterization

Scanning Near-field Optical Microscopy

Time- and spectrally-resolved scanning near-field optical microscopy was applied to study spatial variations of photoluminescence (PL) spectra and carrier dynamics in polar InGaN/GaN single quantum wells (QWs) emitting in a broad spectral range, from 410 nm to 570 nm. The main attention was devoted to variations of the PL properties and carrier dynamics around V-defects. The PL intensity, peak wavelength and linewidth, as well as the radiative and nonradiative recombination times were found to be different in V-defect-rich and defect-free regions. A publication detailing these results has been accepted to Journal of Applied Physics [Yapparov 2020b].

Light-induced Transient Grating

Diffusion coefficient of holes can provide new knowledge about carrier localization in InGaN, where carrier dynamics are altered by randomly fluctuating potential landscape. In III-nitrides, the diffusivity of holes is difficult to measure by electrical methods, but it can be studied using the optical techniques. Here, we investigated the dependence of hole diffusion coefficient on direction and carrier density in *c*-plane and *m*-plane InGaN quantum well structures by employing the light-induced transient grating technique. These results were published in Physical Review Applied [Aleksiejūnas 2020].

Atom Probe Tomography

Throughout this project, we routinely used atom probe tomography (APT) to characterize our epitaxial materials. One such example where we performed extensive APT analysis was for comparing InGaN and GaN quantum barriers. In conjunction with the InGaN barrier device measurements, we performed APT on the six samples (3 samples with GaN barriers + 3 samples InGaN barriers) to measure the In fraction in the QWs and also to investigate any possible differences in the well morphologies. Figure 21, 22 and 23 respectively show the APT results for the single QW samples, the 3 QWs samples and the 5 QWs samples. The top part of each Figure (sub-figures (a) and (b)) show the results for the GaN barrier sample while the bottom part of each Figure (sub-figures (c) and (d)) show the results for the InGaN barrier sample. We are going to comment on few interesting features in some figures but the major results for each sample (compositions of the layers of interest and thicknesses) are all displayed in the table in Figure 24.

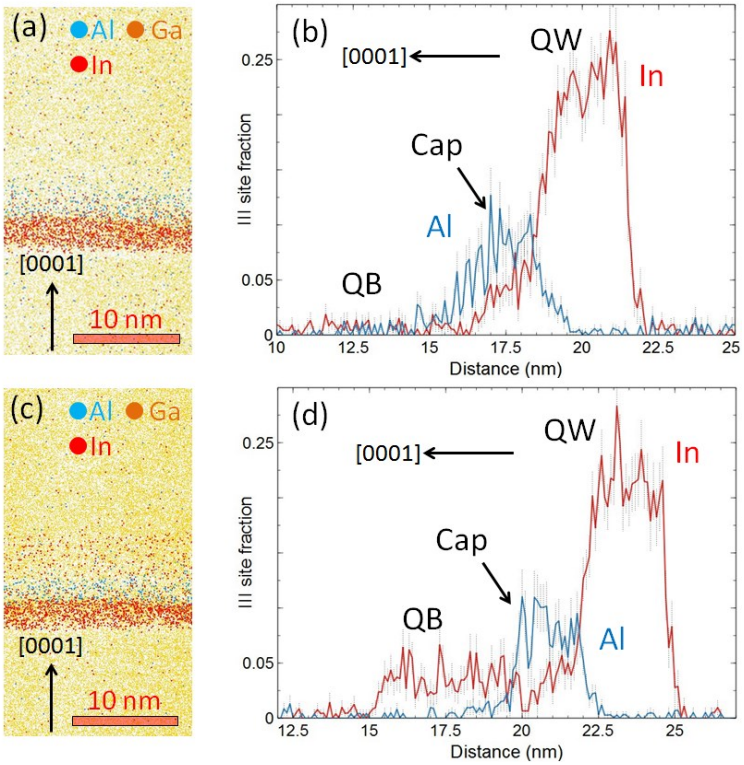

Figure 21. APT 3D reconstructions and 1D concentration profiles showing the active region in two single QW samples. (a-b) QW grown with an InGaN barrier layer. (c-d) QW grown with a GaN barrier layer.

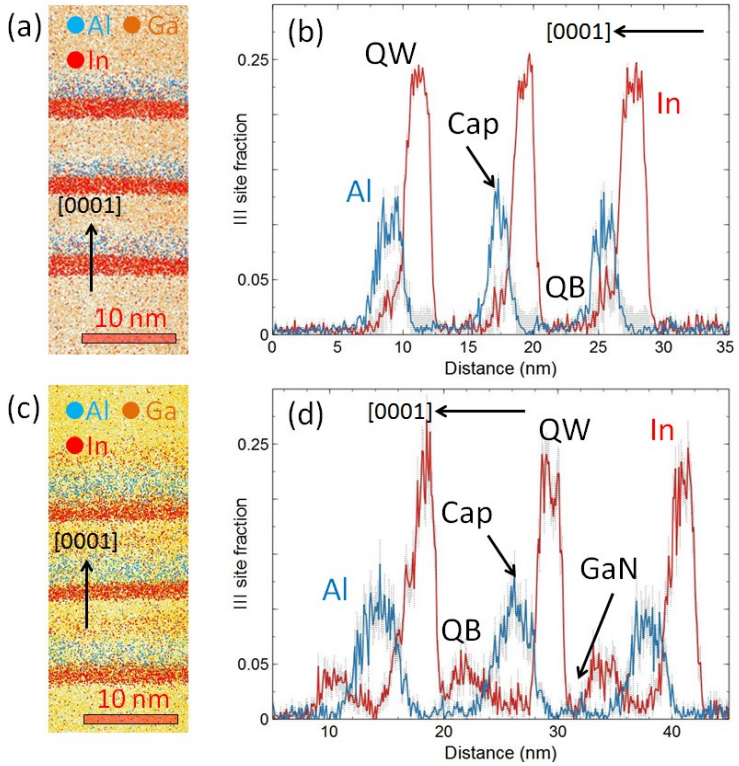

Figure 22. APT 3D reconstructions and 1D concentration profiles showing the active region in two 3 QW samples. (a-b) QWs grown with an InGaN barrier layer. (c-d) QWs grown with a GaN barrier layer.

The interesting feature to notice in Figure 22 is in the InGaN barrier sample. In the 3D APT volume (Figure 22(c)), we noticed that In atoms in the InGaN barrier layer are not observed all the way from the top interface of the AlGaN cap to the bottom interface of the following InGaN QW. This suggests that pure GaN is still present in our barrier layers which was not intended during growth. The barrier layer was supposed to be only composed of InGaN and it was a major input in the 3D simulations performed on InGaN vs GaN barriers. This observation was confirmed using the 1D concentration profile displayed in Figure 22(d). An almost pure GaN layer can be clearly observed in the first grown barrier layer (arrow in Figure 22(d)). We suspect that this is caused by a growth pause between the InGaN QB and subsequent InGaN QW. For now, we are not aware if this is detrimental to the device performance of the and particularly the impact on the turn on voltage compared to a sample having complete InGaN barrier layers.

Similar to the 3QWs sample with the InGaN barrier layers, GaN is observed in the QB also for the 5QWs sample (Figure 23(c) and 23(d)). Also, APT results revealed that for both the 5QWs samples, some Al atoms were detected at the bottom interfaces of the last grown QWs (arrows in Figure 23(b) and 23(d)). This may be caused by the growth pause happening just before the growth of the QWs to decrease the TMI bubbler temperature, which here resulted in the incorporation of Al.

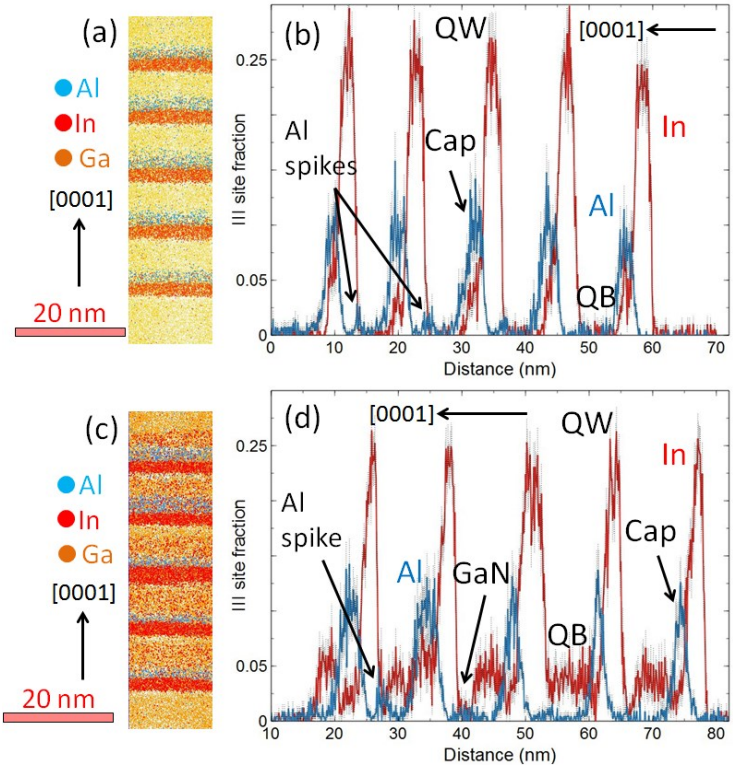

Figure 23. APT 3D reconstructions and 1D concentration profiles showing the active region in two 5QWs samples. (a-b) QWs grown with an InGaN barrier layer. (c-d) QWs grown with a GaN barrier layer.

	Peak In in QW	QW FWHM	Peak Al in cap layer / In in cap	Cap layer FWHM	In in QB	QB thickness
SQW GaN	24%	2.9 nm	8% / 4%	2.9 nm		
SQW InGaN	21%	2.8 nm	9% / 3%	2.2 nm	4%	3.5 nm
3QW GaN	24%	2.1 nm	9% / 3%	2.4 nm		
3QW GaN	24%	1.8 nm	10% / 4%	1.7 nm		
3QW GaN	23%	2.2 nm	9% / 4%	1.9 nm		
3QW InGaN	22%	2.8 nm	9% / 3%	4.1 nm	3%	2.5 nm
3QW InGaN	22%	2.3 nm	9% / 2%	3.7 nm	3%	3.5 nm
3QW InGaN	22%	2.4 nm	8% / 1%	3.3 nm	4%	3.9 nm
5QW GaN	24%	2.7 nm	8% / 5%	2.4 nm		
5QW GaN	24%	2.7 nm	9% / 3%	2.1 nm		
5QW GaN	24%	3.0 nm	9% / 4%	3.7 nm		
5QW GaN	24%	2.7 nm	9% / 4%	2.8 nm		
5QW GaN	23%	2.7 nm	8% / 4%	2.8 nm		
5QW InGaN	24%	2.5 nm	10% / 2%	3.4 nm	5%	4 nm
5QW InGaN	24%	2.8 nm	10% / 5%	3.7 nm	4%	4.2 nm
5QW InGaN	23%	4.0 nm	9% / 4%	2.5 nm	4%	5 nm
5QW InGaN	23%	2.8 nm	9% / 4%	1.5 nm	4%	6.1 nm
5QW InGaN	23%	3.1 nm	9% / 4%	1.5 nm	4%	5.9 nm

Figure 24. Table gathering the QWs, cap layers and barrier layers thicknesses and compositions which were extracted from the 6 APT profiles in Figure 21, 22 and 23.

Figure 24 is a table gathering the compositions of the different layers and their thicknesses. All the results for each QW/cap/QB are respectively displayed with a blue background for the GaN barrier samples and with a grey background for the InGaN barrier samples. Numbers that do not reflect the average trend and can explain the wavelength shift mentioned previously are highlighted in red. It is unsuitable here to draw any conclusions from APT measurements on thickness measurements. Wavelengths in LEDs can shift drastically even for very small fluctuations in QW thicknesses and APT does not have the possibility to give such kind of profiles with a monolayer resolution. First because we cannot resolve atomic planes in the [0001] direction and second because of trajectory artifacts when interfaces between different layers are evaporated. Consequently, here we only pay attention the In fraction measurements in between samples and QWs. The blue shift between the InGaN barrier samples and the GaN barrier samples for the single QW and 3 QWs can be partially explained by the lower In concentrations measured in the QWs between the samples (Figure 24). However, we do not have the ability yet to explain the significant

red shift between the GaN barrier samples with increasing number of QWs since the In fraction in the QWs between the 3 samples is constant.

APT analysis of a MQW green LED with a V-defect was also carried out. The APT 3D reconstruction, along with a schematic showing the approximate shape and location of a V-defect, are shown in Figure 25. Also in Figure 25 is a 1D concentration profile that was taken along the black dashed line shown in the reconstruction. Compared to the high In content of the planar QWs (~22% In) for this green LED, the V-defect sidewall QWs have a much lower indium incorporation.

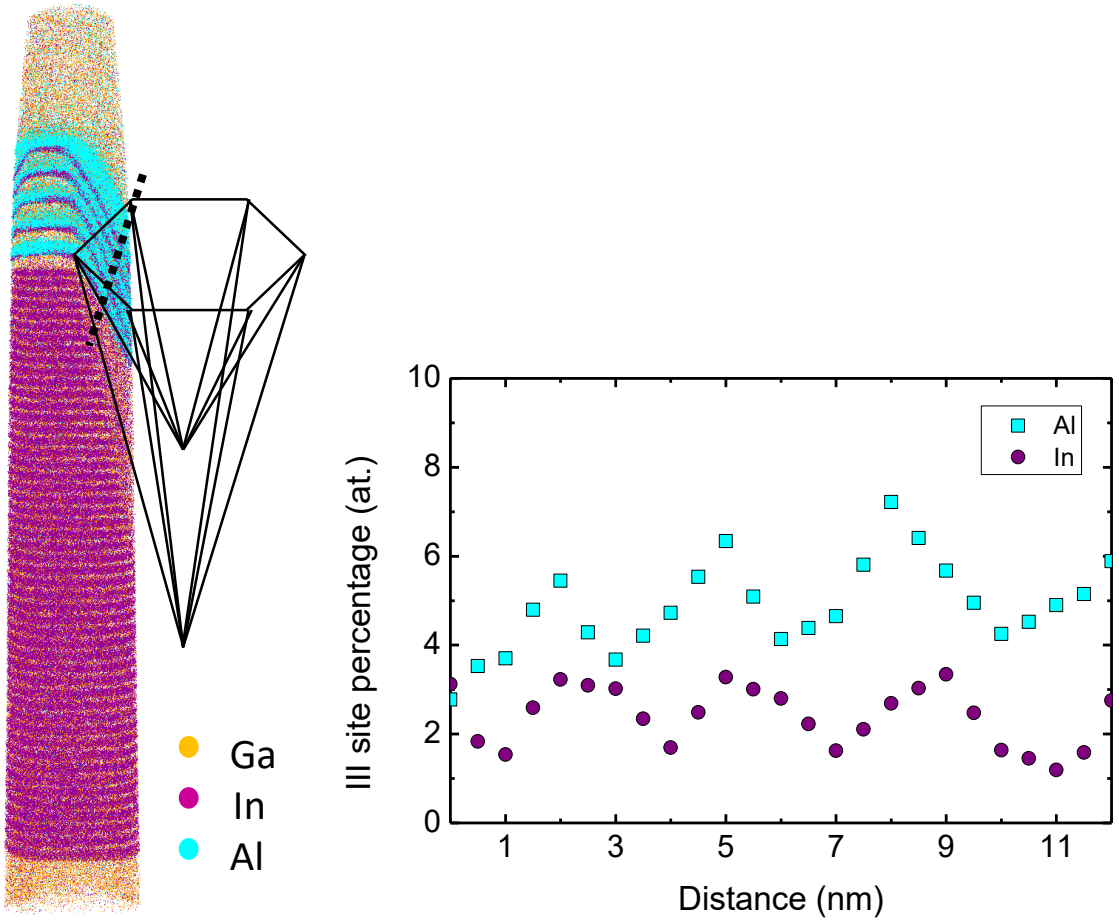

Figure 25. APT 3D reconstructions and 1D concentration profiles showing the active region a 5 QW green LED sample containing a V-defect. The 1D concentration profile is taken along the dashed line and thus shows the Al and In content of the sidewall QWs and capping layers.

Transmission Electron Microscopy

Transmission electron microcopy (TEM) has been an important characterization technique throughout the project and has become even more crucial as we pursue V-defect engineering for high WPE green LEDs. Figure 26 shows high-angle annular dark field (HAADF) images and maps from energy dispersive X-ray spectroscopy (EDS) analysis. Measurements were performed on a 5 QW green LED with a 30-period InGaN/GaN superlattice which serves to initiate V-defects. Images were taken from V-defect free area and an area containing a V-defect which was initiated in the SL. EDS maps were taken for Al, Ga, and In. Figure 27 shows the III-site composition

profile measured from a V-defect free area, where the In composition is approximately 22%. This composition was consistent with those expected based on APT of similar samples.

In Figure 28, we show close up HAADF and EDS images of the V-defect sidewall. From these, it is clear that the sidewall QWs and QBs have a reduced thickness relative to the planar QWs and QBs. Figure 29 again shows the III-site composition profile measured along line 1 (shown in Figure 28) which is in a planar region but close to a V-defect. From this profile, we observed a higher In composition in the QWs, close to 30% In in some regions, compared to the composition from a V-defect free area. Lastly, Figure 30 gives the In composition profile measured along line 2 (shown in Figure 28) which is along the semipolar {10-11} sidewall of a V-defect. Along the sidewall, the In composition has a peak value of approximately 10%, which is significantly lower than the 22% measured in a V-defect free area. These results show the importance of advanced characterization, specifically by TEM, for V-defect engineering. We are continuing our characterization efforts to better understand the changes in indium incorporation in the presence of a V-defect.

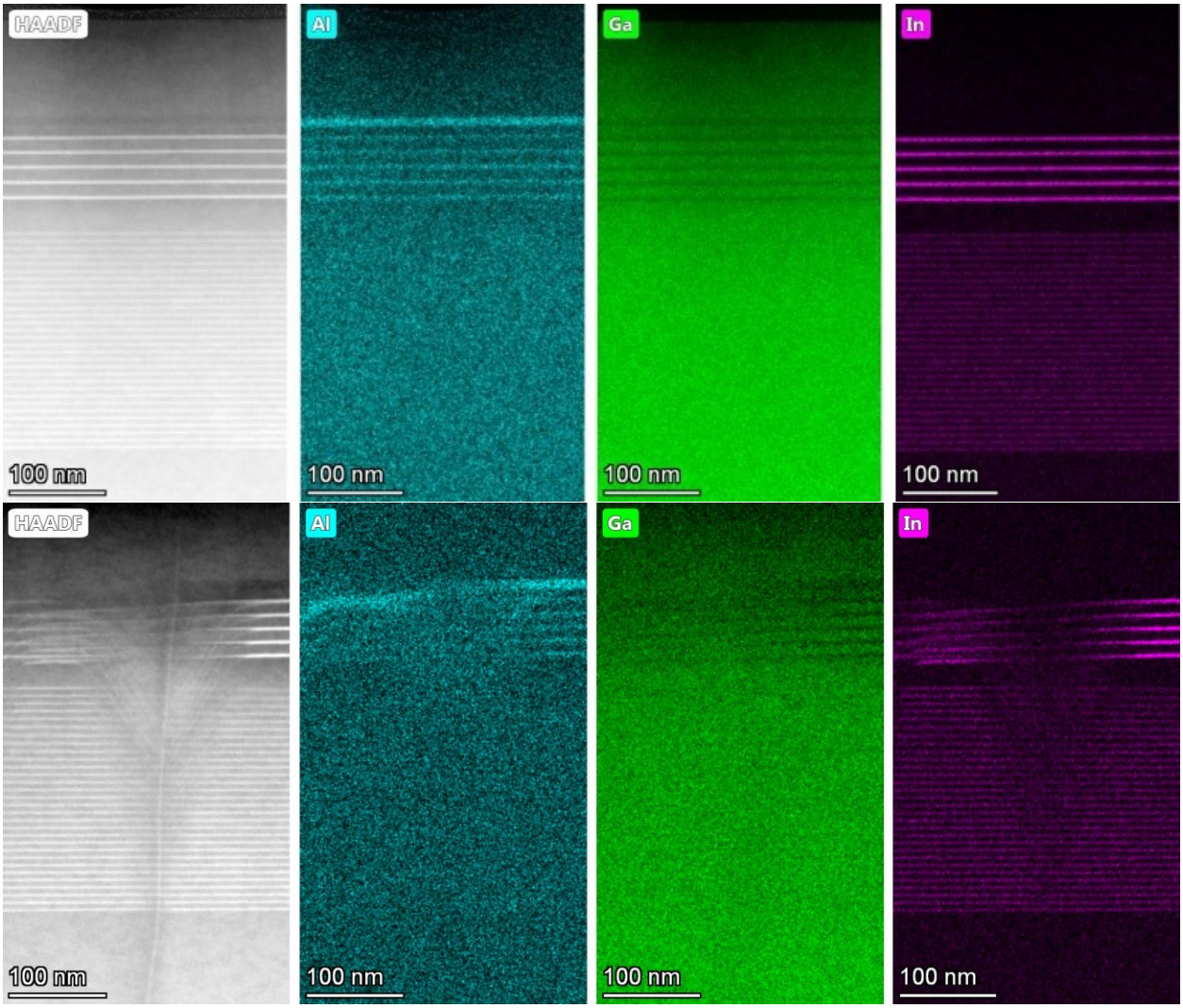

Figure 26. HAADF image and EDS maps of a 5 QW green LED taken from an area without a V-defect (top) and an area with a V-defect (bottom).

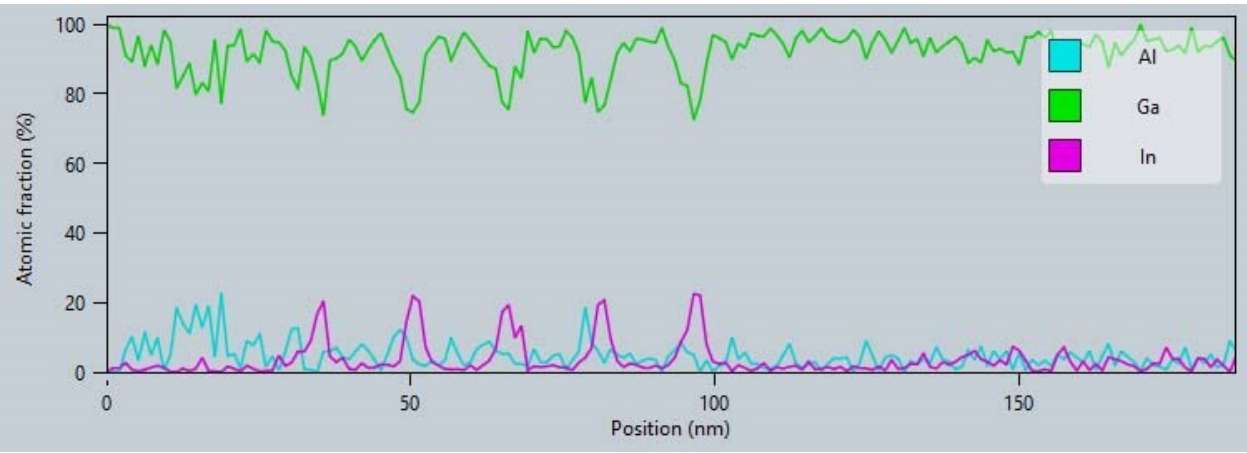

Figure 27. III-site composition profile measured from a V-defect free area.

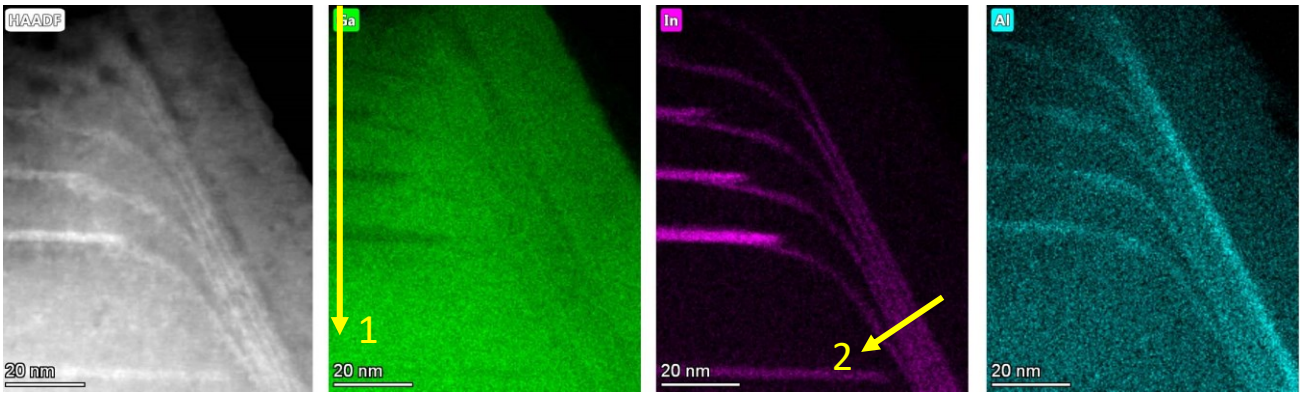

Figure 28. HAADF image and EDS maps showing the V-defect sidewall.

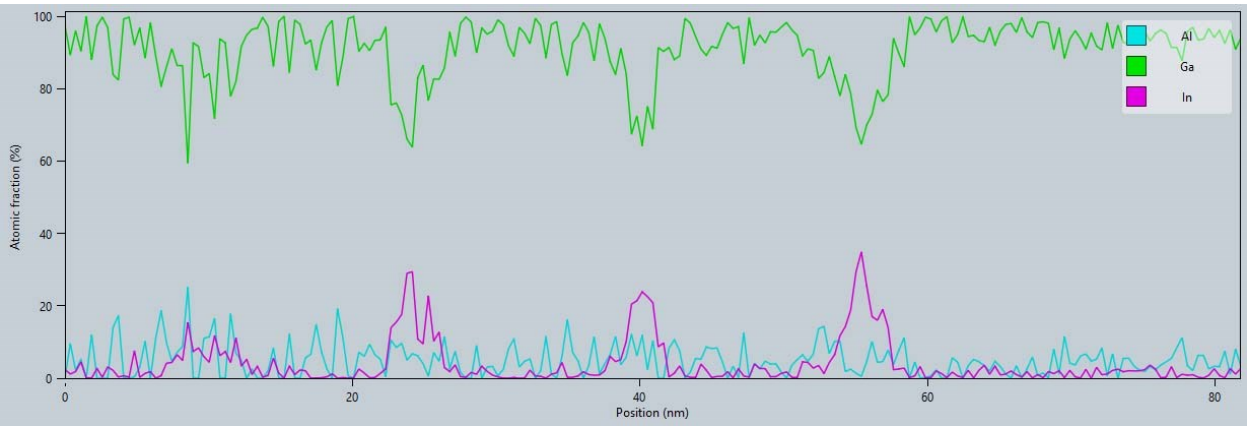

Figure 29. III-site composition profile measured along line 1, given in Figure 28, which is in a planar region but close to a V-defect.

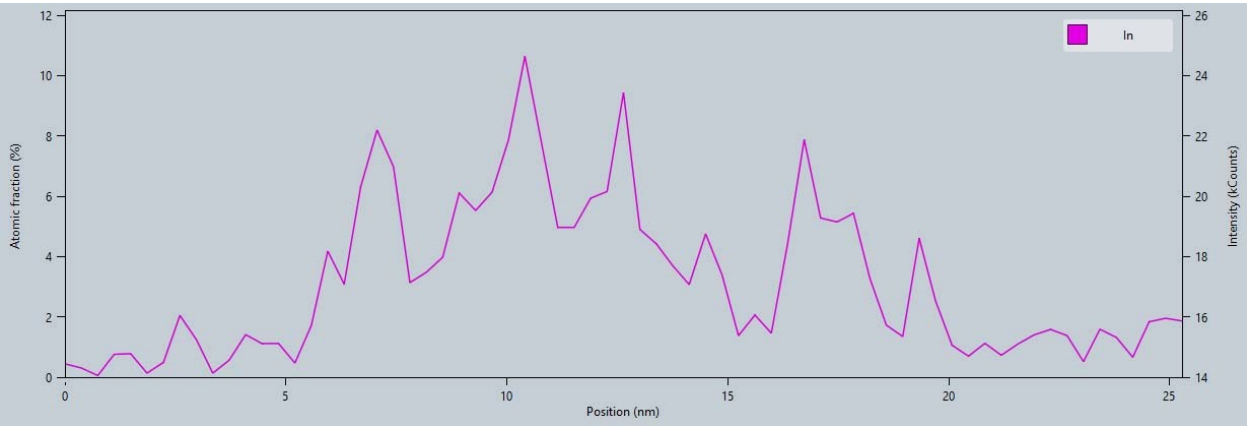

Figure 30. In composition profile measured along line 2, given in Figure 28, which is along the semipolar {10-11} sidewall of a V-defect.

Progress on MOCVD Tunnel Junction Green LEDs

In a typical MOCVD grown LED device, p-GaN is highly resistive due to high activation energy of the Mg acceptor used for p-type doping. This results in poor current spreading from this high resistivity, causing poor only partial mesa emission or other poor emission profiles. Finally, this culminates in significant added voltage. To combat this, typically a current spreading layer is used, most commonly consisting of a transparent conductive oxide (TCO). Current industry standards use Sn-doped In_2O_3 (ITO) as this layer. However, this layer can be replaced by MOCVD-grown n+ GaN to reduce fabrication complexity and offer similar current spreading benefits. While previous work on LED tunnel junctions had focused on MBE regrowth on MOCVD grown samples, MOCVD-grown tunnel junctions have been realized with successful devices. To realize MOCVD-grown tunnel junctions, focused studies on masking and regrowth dimensions of the tunnel junction for activation, activation temperature of p-GaN, and doping schemes were all necessary.

Activation of the underlying p-GaN is necessary for a functional device. Growth of a tunnel junction atop the p-GaN limits the possible device sizes, as activation would rely on sidewall area for H_2 escape and can lead to emission uniformity issues (Figure 31). As a solution, vias can be patterned to allow for H_2 escape during the p-GaN activation anneal. Both a patterned etch of the tunnel junction post-growth (Figure 32) or patterning and depositing dielectric followed by selective-area-growth to regrow the tunnel junction and dielectric removal can be used to create these vias (Figure 33). Ultimately, the patterning and regrowth method is superior to the etching method due to the lack of etch damage but otherwise equivalent surface cleaning, leading to less creation of SRH centers from this damage. Pillars of SiO_2 are created by patterning an as-grown LED using photolithography followed by blanket deposition (Figure 34). After these SiO_2 pillars are formed, selective area growth of the n+ GaN TJ contact is performed in MOCVD. After growth, SiO_2 is removed with BHF, and the p-GaN underneath can then be activated through the newly formed vias (Figure 35).

The effect of pillar spacing and diameter, as well as activation temperature, was used to determine optimal activation conditions based on device voltage and power under operation.

Optimal GaN:Mg activation temperature and time were determined by performing activation under different temperatures on samples with identical pillar diameter and spacing. Power can be compared between the samples with differing activation temperatures at varying current density (Figure 36), ultimately showing 700 °C activation as having the highest power. Additionally, voltage can be compared at a given current density between samples with these activation temperatures and varying pillar spacing (Figure 37), again clearly indicating 700 °C as the superior activation temperature with lower voltage. From these same activation studies, the 3 µm via diameters were chosen as a medium power medium voltage size (rather that high/high or low/low) suitable for most LEDs. The voltage steadily increases as distance between vias increases, while power remains relatively constant as the vias spacing increases from 10-40 µm (Figure 38) causing the 10 µm vias spacing to result in the most efficient device. Eventually as spacing becomes too great, activation becomes incomplete, resulting in lower power, and higher resistivity leading to higher voltage. Ultimately, the optimized via size and spacing results in a device with significantly more uniform emission than devices with reference tunnel junctions without patterns (Figure 39).

Doping schemes were also examined to find the best tunnel junction morphology as well as maximum dopant incorporation for high conductivity. Prior TJs were doped at [Si] = $5x10^{19}$ cm^{-3} using continuous Si_2H_6 flow. For doping the tunnel junction for maximum conductivity, continuous versus pulsed doping schemes were examined, where continuous flow involves flowing the same volume of Si_2H_6 while pulsed doping involves periodically toggling the doping on and off. Typical continuous doping maximizes at [Si] = $1x10^{20}$ cm^{-3} compared to the previously used value of [Si] = $5x10^{19}$ cm^{-3}. Pulsed doping schemes can be used to increase the doping level of the TJ contact over that of continuous doping based on the pulse duration (Figure 40). In addition to an increase of the effective doping level, pulsed doping schemes also result in a smoother surface with RMS roughness decreased by a factor of two (Figure 41). An additional benefit of the pulsed scheme is the ability to grow at lower temperatures, resulting in reduced Mg diffusion from the lower p-GaN into the tunnel junction as it grows (Figure 42). With optimized MOCVD tunnel junction contacts, only a small voltage penalty is taken compared to standard TCO current spreading contact layers, and this penalty has been reduced compared to MBE grown tunnel junctions, resulting in higher wall plug efficiency (Figure 43). Ultimately, the tunnel junction contacts improve efficiency at the cost of only a small voltage penalty when an optimized growth and activation scheme can be reached.

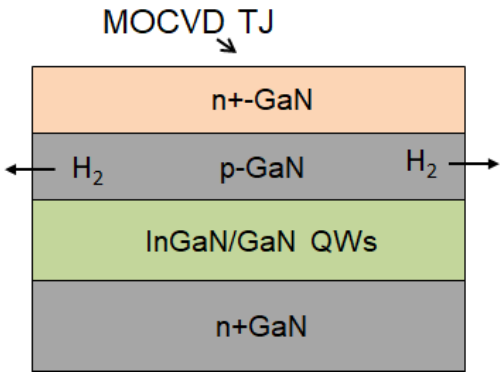

Figure 31. Schematic of restricted activation scheme with as-grown tunnel junction

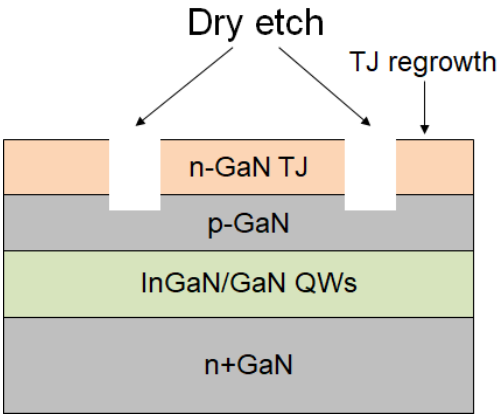

Figure 32. Etching scheme of via formation.

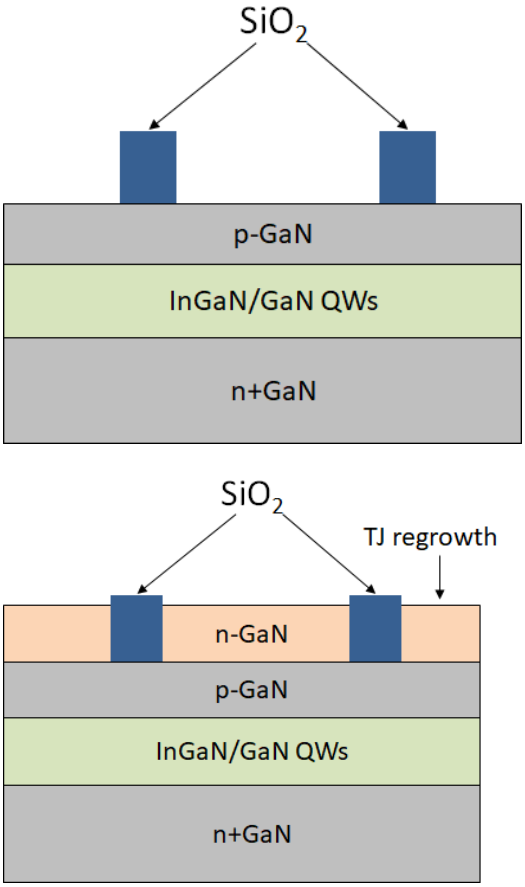

Figure 33. (top) patterning and (bottom) selective area regrowth scheme of via formation

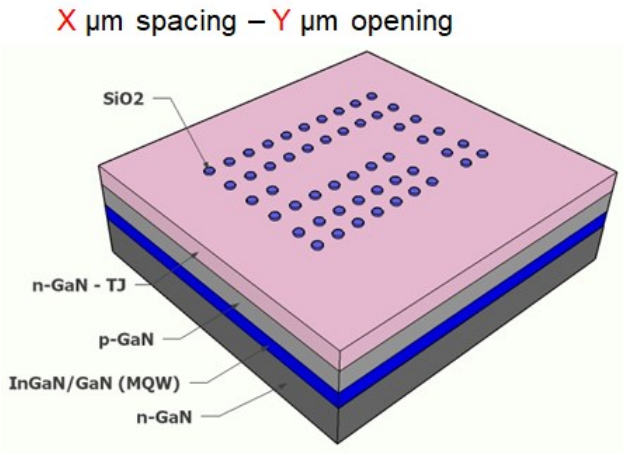

Figure 34. Schematic of via patterning for LED device.

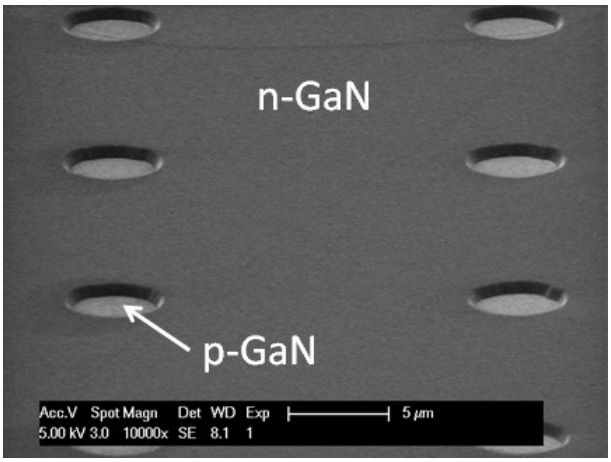

Figure 35. SEM image of patterned vias after SiO_2 removal.

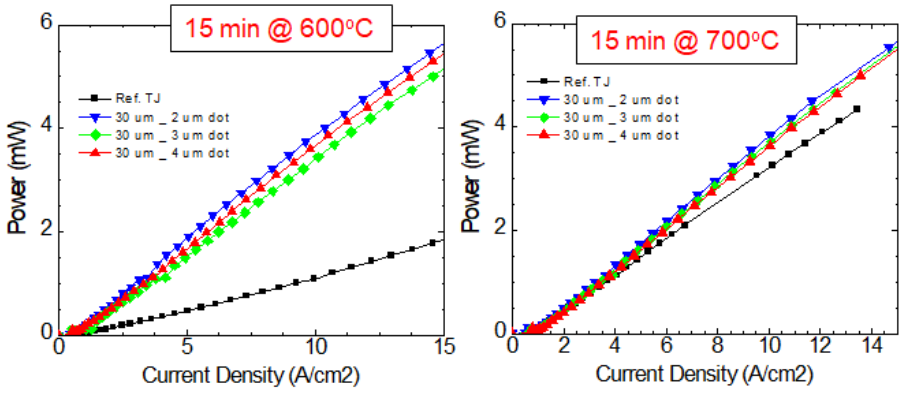

Figure 36. Comparison of power versus current density for different activation temperatures and patterns.

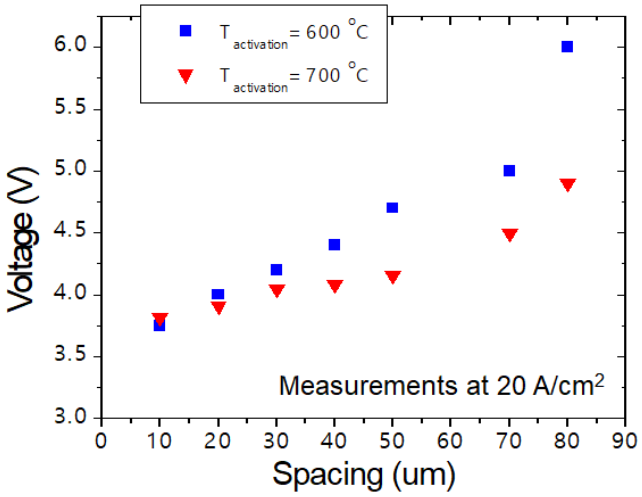

Figure 37. Comparison of voltage at 20 A cm^{-2} for varying via spacings and different activation temperatures.

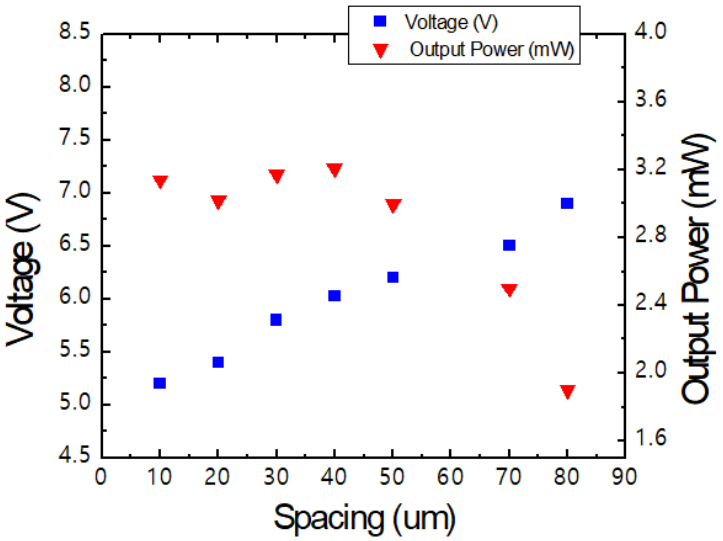

Figure 38. Comparison of voltage and power for varying via spacings.

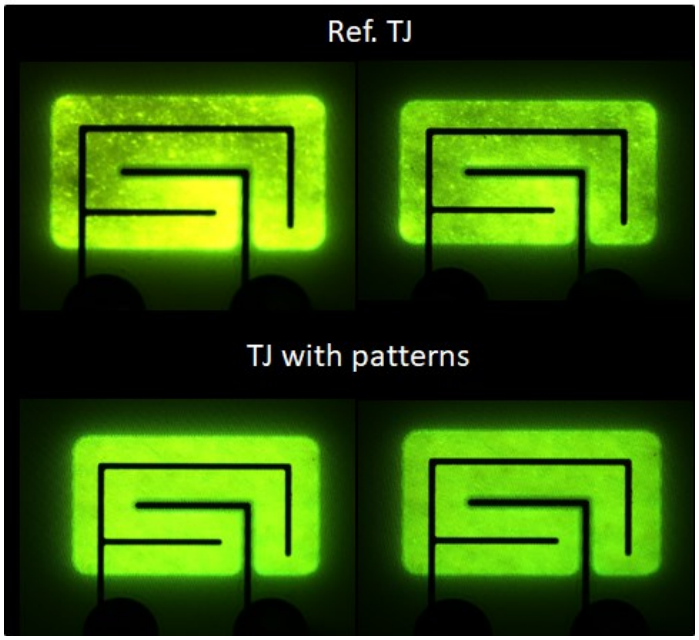

Figure 39. Optical image of emission uniformity for reference tunnel junction (without patterning) and optimized pattern tunnel junction

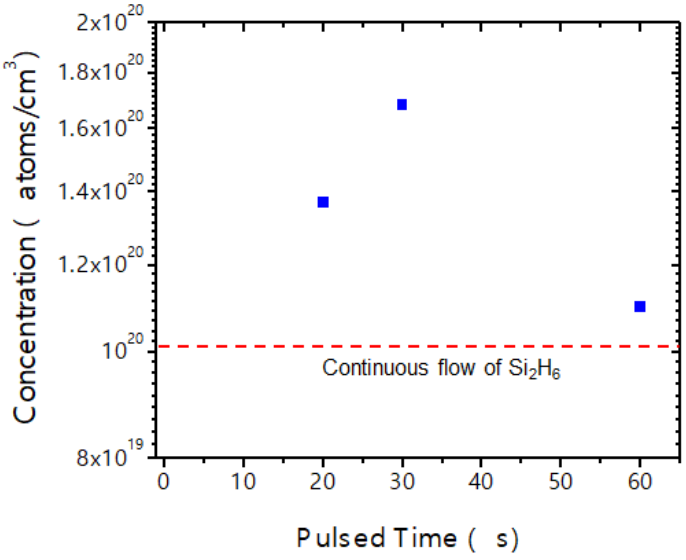

Figure 40. Si dopant incorporation based on length of dopant pulse. Continuous flow level shown for reference.

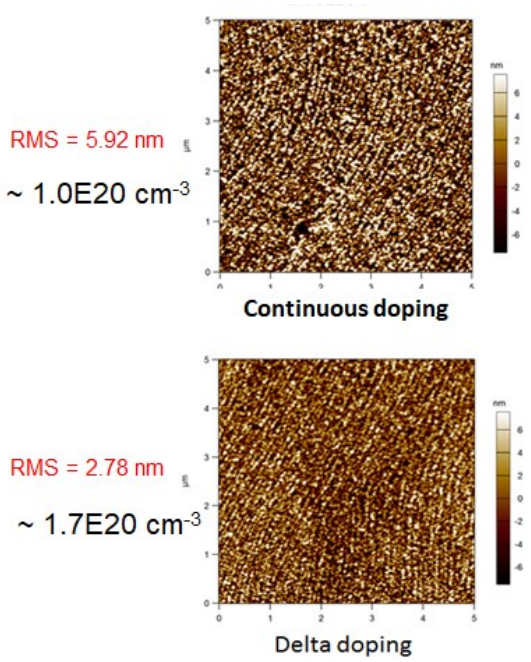

Figure 41. AFM images of continuous doping (top) and pulsed doping (bottom) scheme TJ surfaces. RMS roughness and doping level shown for reference.

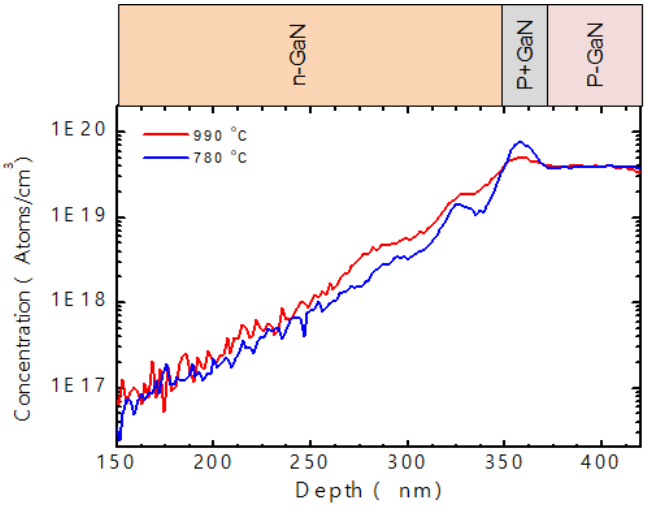

Figure 42. SIMS of Mg in TJ grown at different temperatures.

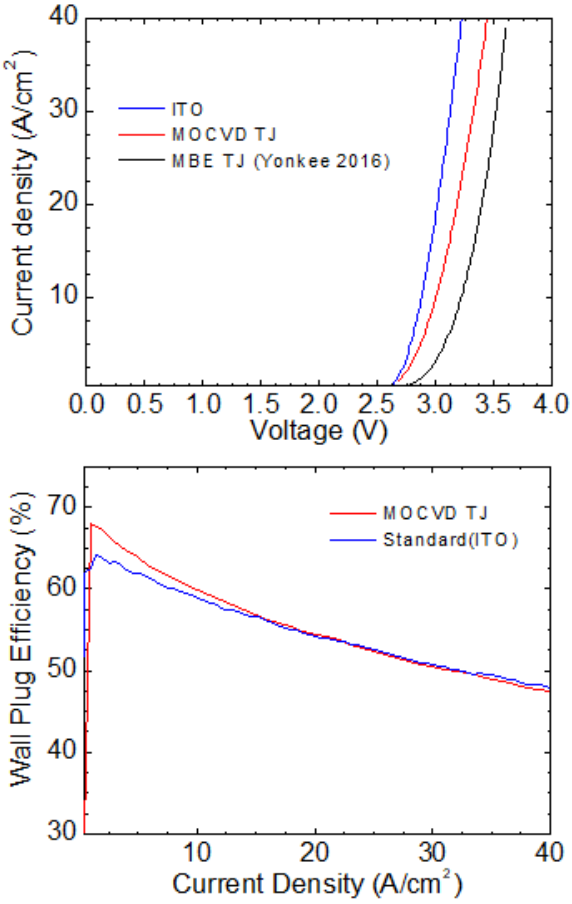

Figure 43. J-V curves (top) and wall plug efficiency (bottom) of LEDs with different current spreading layer schemes.

References

[Aleksiejūnas 2020] R. Aleksiejūnas, K. Nomeika, O. Kravcov, S. Nargelas, L. Kuritzky, C. Lynsky, S. Nakamura, C. Weisbuch, and J. S. Speck, "Impact of Alloy-Disorder-Induced Localization on Hole Diffusion in Highly Excited c-Plane and m-Plane (In,Ga)N Quantum Wells," Phys. Rev. Applied **14**(5), 054043 (2020).

[Hangleiter 2005] A. Hangleiter, F. Hitzel, C. Netzel, D. Fuhrmann, U. Rossow, G. Ade, and P. Hinze, "Suppression of Nonradiative Recombination by V-Shaped Pits in GaInN / GaN Quantum Wells Produces a Large Increase in the Light Emission Efficiency," Phys. Rev. Lett. **95**(12), 127402 (2005).

[Jiang 2019] F. Jiang, J. Zhang, L. Xu, J. Ding, G. Wang, X. Wu, X. Wang, C. Mo, Z. Quan, X. Guo, C. Zheng, S. Pan, and J. Liu, "Efficient InGaN-based yellow-light-emitting diodes," Photonics Res. **7**(2), 144–148 (2019).

[Lheureux 2020] G. Lheureux, C. Lynsky, Y.-R. Wu, J. S. Speck, C. Weisbuch, and J. S. Speck, "A 3D simulation comparison of carrier transport in green and blue c-plane multi-quantum well nitride light emitting diodes," J. Appl. Phys. *Accepted* (2020).

[Lynsky 2020] C. Lynsky, A. I. Alhassan, G. Lheureux, B. Bonef, S. P. DenBaars, S. Nakamura, Y.-R. Wu, C. Weisbuch, and J. S. Speck, "Barriers to carrier transport in multiple quantum well nitride-based c -plane green light emitting diodes," Phys. Rev. Materials **4**(5), 054604 (2020).

[Myers 2020] D. J. Myers, A. C. Espenlaub, K. Gelzinyte, E. C. Young, L. Martinelli, J. Peretti, C. Weisbuch, and J. S. Speck, "Evidence for trap-assisted Auger recombination in MBE grown InGaN quantum wells by electron emission spectroscopy," Appl. Phys. Lett. **116**(9), 091102 (2020).

[Quan 2014] Z. Quan, L. Wang, C. Zheng, J. Liu, and F. Jiang, "Roles of V-shaped pits on the improvement of quantum efficiency in InGaN/GaN multiple quantum well light-emitting diodes," J. Appl. Phys. **116**(18), 183107 (2014).

[Quan 2015] Z. Quan, J. Liu, F. Fang, G. Wang, and F. Jiang, "A new interpretation for performance improvement of high-efficiency vertical blue light-emitting diodes by InGaN/GaN superlattices," J. Appl. Phys. **118**(19), 193102 (2015).

[Wu 2015] X. Wu, J. Liu, and F. Jiang, "Hole injection from the sidewall of V-shaped pits into c-plane multiple quantum wells in InGaN light emitting diodes," Journal of Applied Physics **118**(16), 164504 (2015).

[Yapparov 2020a] R. Yapparov, C. Lynsky, S. Nakamura, J. S. Speck, and S. Marcinkevičius, "Optimization of barrier height in InGaN quantum wells for rapid interwell carrier transport and low nonradiative recombination," Appl. Phys. Express **13**(12), 122005 (2020).

[Yapparov 2020b] R. Yapparov, Y. C. Chow, C. Lynsky, F. Wu, S. Nakamura, J. S. Speck, and S. Marcinkevičius, "Variations of light emission and carrier dynamics around V-defects in InGaN quantum wells," J. Appl. Phys. *Accepted* (2020).

Project output

Publications

1. R. Aleksiejūnas, K. Nomeika, O. Kravcov, S. Nargelas, L. Kuritzky, C. Lynsky, S. Nakamura, C. Weisbuch, and J. S. Speck, "Impact of Alloy-Disorder-Induced Localization on Hole Diffusion in Highly Excited c-Plane and m-Plane (In,Ga)N Quantum Wells," Phys. Rev. Applied **14**(5), 054043 (2020).
2. G. Lheureux, C. Lynsky, Y.-R. Wu, J. S. Speck, C. Weisbuch, and J. S. Speck, "A 3D simulation comparison of carrier transport in green and blue c-plane multi-quantum well nitride light emitting diodes," J. Appl. Phys. *Accepted* (2020).

3. C. Lynsky, A. I. Alhassan, G. Lheureux, B. Bonef, S. P. DenBaars, S. Nakamura, Y.-R. Wu, C. Weisbuch, and J. S. Speck, "Barriers to carrier transport in multiple quantum well nitride-based c -plane green light emitting diodes," Phys. Rev. Materials **4**(5), 054604 (2020).
4. R. Yapparov, C. Lynsky, S. Nakamura, J. S. Speck, and S. Marcinkevičius, "Optimization of barrier height in InGaN quantum wells for rapid interwell carrier transport and low nonradiative recombination," Appl. Phys. Express **13**(12), 122005 (2020).
5. R. Yapparov, Y. C. Chow, C. Lynsky, F. Wu, S. Nakamura, J. S. Speck, and S. Marcinkevičius, "Variations of light emission and carrier dynamics around V-defects in InGaN quantum wells," Journal of Applied Physics **128**(22), 225703 (2020).

Publications in progress

1. C. Lynsky, G. Lheureux, B. Bonef, S. P. DenBaars, S. Nakamura, Y.-R. Wu, C. Weisbuch, and J. S. Speck, "Impact of alloy disorder in InGaN quantum barriers on carrier transport and device performance of III-nitride green LEDs," *In preparation*.
2. C. Lynsky, S. Nakamura, S. P. DenBaars, and J. S. Speck, "Voltage reduction in green LEDs on sapphire substrates using engineered V-defects," *Under review*.
3. F. Wu, C. Lynsky, S. P. DenBaars, S. Nakamura, and J. S. Speck, "Microstructural characterization and compositional analysis of V-defects in InGaN green LEDs," *In preparation*.

Oral conference presentations

1. I. Alhassan, "Realization of MOCVD GaN tunnel junctions contacts in large area LEDs," presented at International Workshop on Nitride Semiconductors 2018 (IWN 2018), Kanazawa, Japan (November 2018).
2. G. Lheureux, "Path towards improved wall-plug efficiency of InGaN green LEDs," presented at International Workshop on Nitride Semiconductors 2018 (IWN 2018), Kanazawa, Japan (November 2018).
3. C. Lynsky, "Contribution of polarization-induced barriers to excess forward voltage in c-plane green LEDs," presented at 13th International Conference on Nitride Semiconductors 2019 (ICNS-13), Bellevue, WA (July 2019).

Patents

1. M. Monavarian, C. Weisbuch, C. Lynsky, G. Lheureux, and J. S. Speck, "Methods of volumetric hole injection via intentional V-defects in Indium Aluminum Gallium Nitride light-emitting diodes," US Patent Application UC Case No. 2020-058, 2019, (Filed).